Journal of
Manufacturing and Materials Processing

MDPI

Article

The Dispersion-Strengthening Effect of TiN Nanoparticles Evoked by Ex Situ Nitridation of Gas-Atomized, NiCu-Based Alloy 400 in Fluidized Bed Reactor for Laser Powder Bed Fusion

Jan-Philipp Roth [1,*], Ivo Šulák [2], Markéta Gálíková [2,3], Antoine Duval [4], Germain Boissonnet [4], Fernando Pedraza [4], Ulrich Krupp [5] and Katrin Jahns [1]

1 Faculty of Engineering and Computer Science, Osnabrück University of Applied Sciences, 49076 Osnabrück, Germany; k.jahns@hs-osnabrueck.de
2 Institute of Physics of Materials, Czech Academy of Sciences, 61600 Brno, Czech Republic; sulak@ipm.cz (I.Š.); galikova@ipm.cz (M.G.)
3 CEITEC—Central European Institute of Technology, Brno University of Technology, 62100 Brno, Czech Republic
4 Laboratoire des Sciences de l'Ingénieur Pour l'Environnement (LaSIE), Université de La Rochelle, 17042 La Rochelle, France; antoine.duval@univ-lr.fr (A.D.); germain.boissonnet@univ-lr.fr (G.B.); fpedraza@univ-lr.fr (F.P.)
5 Steel Institute IEHK, RWTH Aachen University, 52072 Aachen, Germany; krupp@iehk.rwth-aachen.de
* Correspondence: j.roth@hs-osnabrueck.de

Abstract: Throughout recent years, the implementation of nanoparticles into the microstructure of additively manufactured (AM) parts has gained great attention in the material science community. The dispersion strengthening (DS) effect achieved leads to a substantial improvement in the mechanical properties of the alloy used. In this work, an ex situ approach of powder conditioning prior to the AM process as per a newly developed fluidized bed reactor (FBR) was applied to a titanium-enriched variant of the NiCu-based Alloy 400. Powders were investigated before and after FBR exposure, and it was found that the conditioning led to a significant increase in the TiN formation along grain boundaries. Manufactured to parts via laser-based powder bed fusion of metals (PBF-LB/M), the ex situ FBR approach not only revealed a superior microstructure compared to unconditioned parts but also with respect to a recently introduced in situ approach based on a gas atomization reaction synthesis (GARS). A substantially higher number of nanoparticles formed along cell walls and enabled an effective suppression of dislocation movement, resulting in excellent tensile, creep, and fatigue properties, even at elevated temperatures up to 750 °C. Such outstanding properties have never been documented for AM-processed Alloy 400, which is why the demonstrated FBR ex situ conditioning marks a promising modification route for future alloy systems.

Keywords: Alloy 400; fluidized bed reactor; laser powder bed fusion; internal nitridation; TiN nanoparticle; dispersion strengthening

Citation: Roth, J.-P.; Šulák, I.; Gálíková, M.; Duval, A.; Boissonnet, G.; Pedraza, F.; Krupp, U.; Jahns, K. The Dispersion-Strengthening Effect of TiN Nanoparticles Evoked by Ex Situ Nitridation of Gas-Atomized, NiCu-Based Alloy 400 in Fluidized Bed Reactor for Laser Powder Bed Fusion. *J. Manuf. Mater. Process.* **2024**, *8*, 223. https://doi.org/10.3390/jmmp8050223

Academic Editor: Hamed Asgari

Received: 4 September 2024
Revised: 27 September 2024
Accepted: 29 September 2024
Published: 2 October 2024

1. Introduction

For many industries, such as the energy, maritime, and chemistry sectors, the fcc solid solution Ni-30Cu-based Alloy 400 (Monel 400) is the material of choice [1,2]. Here, the alloy finds its application as heat exchangers, feedwater/steam-containing heater tubes, reinforcements of offshore installations, and evaporators in both oxidizing (e.g., nitric acid) and reducing (e.g., alkaline salts, phosphoric acid) environments, even at higher temperatures [2–5]. Alloy 400 consists of approximately two-thirds of Ni, one-third of Cu, and, in small and decreasing proportion, Fe, Si, Mn, Al, and C. Similar alloys used for alternative applications are the related age-hardenable K500 (rather used as a high-strength variant for freshwater- and seawater-related corrosion) and the binary Ni-50Cu (enhanced stability during metal dusting in carburizing atmospheres) [2,3,6]. Hence, incorporating

further benefits in a strengthened Alloy 400 variant to withstand the harsh environments of the various demanding sectors while not losing its characteristic properties is considered an urgent need. In utilizing the respective benefits of additive manufacturing and the dispersion-strengthening effect, such superior parts could be produced and, thus, product lifetimes extended [7,8]. This idea was elaborated in a previous work [9] based on a gas atomization reaction synthesis [10–13]. Designing a modified Alloy 400 that exceeds the good properties reached via the GARS method is the main aim of this study.

Additive manufacturing still reveals plenty of drawbacks when compared to conventional fabrication: investment costs are comparatively high, geometrical precision is often lacking, and, due to the high cooling rates during solidification, immense induced residual stresses occur [14,15]. Also, the process-related anisotropy in the build direction is difficult to avoid or compensate for [16–18]. Yet, the advantages of this manufacturing route are manifold. For instance, since there is no need for geometry-specific tools and consecutive manufacturing steps, the part costs are very low for small and medium batch sizes, allowing for many different product variants of near-net shape (customization for free) [14,16,19]. Also, as three-dimensional tasks are divided into two-dimensional layers, the costs per part are independent of its complexity (complexity for free), which is why the design can iteratively be adjusted at no extra costs [14,16,20]. Besides economic benefits, there are also specific advantages concerning the microstructural condition of the manufactured part as it can be tailored to its specific need. Here, an AM technique of special interest for the material design of Ni-based materials is the laser-based powder bed fusion of metals (PBF-LB/M as per standard DIN EN ISO/ASTM 52900), also frequently referred to as laser powder bed fusion (LPBF), an iterative and selective micro-welding process of a powder bed resulting in a layer-wise solidified part [21–24]. Via LPBF, a controlled and consistent solidification of the melt pool to fine grains throughout the whole geometry can be achieved [25]. Also, it allows for printed parts with a relatively high-resolution surface quality [21]. Most importantly, LPBF allows for the processing of nanoparticle (NP)-reinforced powder feedstocks, as intended throughout this work as well [7,25,26].

A current, very promising approach at the intersection of materials science and AM is the homogenous introduction of such nanoparticles on the sub-grain level, enabling for equiaxed grains and, thus, restricting anisotropy as normally present with production-related columnar grains [7,25]. The intention is to enhance the mechanical performance of these dispersion-strengthened alloy systems due to dislocation pinning or climbing (Orowan mechanism) at the respective NPs when under load [7,26,27]. Moreover, NP dispersion strengthening can be considered a very effective strengthening mechanism as the NPs are not only beneficial to the material performance themselves but also come with some indirect effects. For instance, they act as nuclei for a more pronounced growth of fine grains during the LPBF liquid–solid phase transformation, which in turn restricts cracking and increases mechanical performance [8,28,29]. Another result is strengthening due to a high number of grain boundaries (GB) and a more pronounced geometrically necessary dislocation (GND) formation [8,30]. As an ultimate result, NP-strengthened alloys exhibit higher static strength, such as an enhanced ultimate tensile strength associated with longer fatigue and creep lifetime, as adequately reported in the literature, even within an increased temperature regime [7,31–35]. The underlying mechanism of evoking NPs is related to the free energy of formation in reactive atmospheres [31,36–38]. Considering the components of the modified Alloy 400 and in accordance with the respective Gibbs free energy over the entire temperature range, TiN is the most likely candidate for NP emergence, with Al_2O_3 being considered a possible one as well although to a much lesser extent, as the experiments were carried out in non-oxidizing argon and nitrogen atmospheres, respectively.

A preceding work [9] introduced the topic of TiN NP modification of the present Alloy 400 during nitrogen gas atomization, which is referred to as in situ, as the nitridation occurs during the liquid–solid phase transition of the melt to powders during atomization. It was demonstrated that Alloy 400 GARS is a feasible concept for providing a TiN-enriched, well-processible powder feedstock for laser powder bed fusion, which in turn results in

an even more pronounced nanoparticle formation in additively manufactured parts. The in situ processed alloy led to a comparable mechanical performance to conventionally fabricated reference material and outperformed the unmodified LPBF material in terms of tensile and creep properties. Still, to reduce porosity issues and increase the NP content in as-built parts even further, a new kind of TiN-enriched material could potentially surpass the performance of the conventional counterpart. For instance, Tjong demonstrated that increasing the Al_2O_3 NP volume percentage in an Al composite material from 1% up to 4% would result in a steadily increasing yield and tensile strength [39]. Therefore, this research focuses on a novel treatment of Alloy 400 powders resulting from standard vacuum inert gas atomizations (VIGA) in close-coupled atomization (CCA) mode and a subsequent modification of the powders in a fluidized bed reactor. During this process, the powder is set to a nitrogen atmosphere to allow for the formation of TiN NPs at a high quantity, detached from the atomization process. Hence, as the phase transformation and the nitridation of powders are divided into successive sections, this approach is referred to as ex situ. Results of this new powder preparation approach are accompanied by a comparison between both modification routes, the in situ one and the ex situ one, and their respective peculiarities are set in relation and also against the background of unmodified LPBF-processed material. Table 1 provides an initial overview of the key distinguishing features between the in situ and the ex situ approaches. The latter is further split up into the pre (atomized but no FBR) and the post (both atomized and FBR) states.

Table 1. Comparison of the in situ and ex situ nitridation approaches for Alloy 400.

	In Situ Nitridation [9]	**Pre-FBR Ex Situ Nitridation [This Work, Sections 3.1 and 3.3]**	**Post-FBR Ex Situ Nitridation [This Work, Sections 3.2–3.4]**
Atomization type	GARS (nitrogen) CCA	Shielding gas (argon) CCA	-
Post-treatment	-	-	FBR (nitrogen)
Targeted NPs in powder	TiN	None	TiN
Targeted NPs in LPBF part	TiN	None	TiN

2. Materials and Methods

2.1. Gas Atomization

The LPBF powder feedstock was generated via gas atomization with an AUG1000HTC atomizer (Blue Power/Indutherm) under a full inert gas atmosphere (argon) present in both the spray tower and the melting chamber. Bulky material consisting of pure elements and binary pre-alloys was molten in an alumina crucible via induction heating of a surrounding graphite crucible. The chemical composition of standard Alloy 400 (approx. 65.0 wt.-% Ni, 31.5 wt.-% Cu, 2.0 wt.-% Fe, 1.0 wt.-% Mn, 0.2 wt.-% Si, 0.2 wt.-% Al, 0.1 wt.-% C) was enriched with titanium in the form of a CuTi30 pre-alloy. The liquidus temperature for Alloy 400 + Ti was calculated at approximately 1350 °C, and an overheating of ~300 °C was applied, adding up to an atomization temperature of 1650 °C. A close-coupled setup was applied, meaning that the melt was atomized to powder right after flowing out of the crucible nozzle, which allows for a narrow, fine particle size distribution and thus increases the yield of usable powder. Besides overheating, a 5 min holding at atomization temperature was applied to homogenize the alloy and to allow for a sufficiently low viscosity of the melt, leading to a smooth flow during atomization. Powders were further processed via sieving and air-classifying in order to adjust the intended final particle size distribution (PSD) for LPBF in the range between 15 µm and 63 µm. For this purpose, a sieving unit (Russell/EOS) and an air classifier AC1000G (Blue Power/Indutherm) were operated. Dynamic image analysis (Camsizer X2) was applied to verify the obtained PSD and to adjust the classifier parameters accordingly.

2.2. Fluidized Bed Reactor

The fluidized bed reactor process is a newly developed method of the LaSIE laboratory, University of La Rochelle, France (patent number: FR2311060), and it causes both surface and internal nanoparticle formation in metal matrix powders. A gas flow is introduced from the bottom of the plenum, which homogenizes and heats the gas before it contacts the micro-sized metal particles. The latter are retained by a porous filter plate through which the gas blows up the particles (Figure 1). During the exposure of the base alloy to the nitriding gas composition at high temperatures, nitridation of the more reactive elements occurs from the surface to the core of the metal particle following a diffusion-controlled mechanism. Therefore, the longer the exposure, the deeper the NP formation occurs in the metal powders. Ultimately, the efficiency of the process depends on several parameters, such as:

- The chemical composition of the powder and the gas: reactive elements with preferably low free energy of formation result in a high number of NPs,
- The initial particle size distribution of the powders: the coarser the powder, the longer it takes for the internal NP formation to fully occur throughout the whole particle,
- Their shape, sphericity and density: highly spherical and dense particles allow for homogeneous gas penetration,
- The temperature applied to the chamber: high diffusion rates correlate with increasing temperature, while disintegration of the particles due to tremendous heat exposure must be avoided.

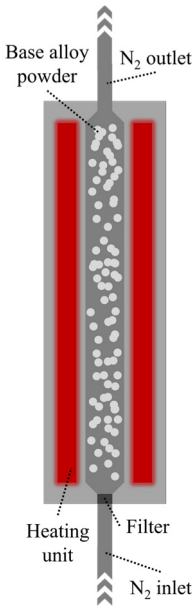

Figure 1. Fluidized bed reactor with nitrogen gas stream, heating unit, and exposed powder.

As a result of a preliminary feasibility study, several FBR process parameter sets were tested in the temperature range of 600 °C to 800 °C at different durations. Here, it was found to be most effective to apply a temperature of 800 °C under a pure nitrogen gas flow of 1.2 L/min over 4 h to the exposed Alloy 400 powders. The heating and cooling process steps were regulated with an argon gas flow.

2.3. Laser Powder Bed Fusion

After atomization and FBR exposure, the powders were used as the LPBF feedstock. For manufacturing, an EOS M290 customized by AMCM was operated, providing several peculiarities for AM material qualification. The laser system operated at a comparably low wavelength of 532 nm (green laser source) to allow for more effective energy incorporation

into the reflective material. It also had a heated build platform of 10 cm in diameter for small powder batches. During manufacturing, a constant heating of 80 °C as well as a layer height of 0.02 mm were applied. The laser traveled according to a rotating scanning strategy (67°) in between layers. The system was fully pressured with argon shielding gas. The parameters were laser power (p_L), scanning speed (s_S), and hatch distance (d_H). For parameter optimization, previously found start values of p_L = 85 W, s_S = 1050 mm/s, and d_H = 50 µm were set and further varied to obtain highly dense parts [9]. In the M290 system, the following components were manufactured during this study:

- Cubes (8 × 8 × 8 mm^3) for optical density measurements (VDI 3405-2), hardness testing (DIN EN ISO 6507-1), and part characterization;
- Blocks (14 × 45 × 70 mm^3) for subsequent machining of tensile, fatigue, and creep specimens:
    - o Tensile and fatigue specimens resulted from M6 × 40 mm cylinders and revealed a final test area of Ø 3 mm × 9 mm (see [40,41] for sample illustration);
    - o Creep specimens were obtained from 41 × 14 × 3.2 mm^3 cuboids and machined to a test area of 25 × 4 × 3.2 mm^3 (see [40,41] for sample illustration);
- Cylinders (Ø 10 mm × 50 mm) for thermal diffusivity testing.

2.4. Testing and Characterization

Vickers hardness measurements were performed on as-printed surfaces and averaged (Innovatest Falcon 500). Cubes for optical density determination via light optical microscopy were first ground (2500 grit SiC) and then further polished (0.02 µm colloidal SiO_2 suspension) for scanning electron microscopy (SEM) investigations. For SEM characterization, a Zeiss Auriga system was operated, and chemical compositions of the various powder and part states were examined via energy dispersive x-ray spectroscopy (EDS). Electron backscattered diffraction (EBSD) was used for grain and dislocation evolution characterization. High-resolution characterization on the nanoscale was performed by utilizing a Talos F200i transmission electron microscope (TEM) at an acceleration voltage of 200 kV with a built-in bright field detector, facilitating the operation in scanning mode (STEM). TEM samples (thin lamellae) were generated via focused $(Ga)^+$ ion beam milling (FIB) in SEM and micro-welded to an omniprobe grid (see [9] for the standard lamella preparation procedure). For mechanical investigations, a universal electromechanical tensile machine Zwick Z50, a servo-hydraulic fatigue testing system MTS810 [40], and a self-designed creep machine [42] were operated. The thermal diffusivity was determined using high-temperature laser-flash measurements with a Linseis LFA1600 apparatus at low pressure (~10^{-2} mbar) and at 100 °C intervals between room temperature and 900 °C. Three coupon samples (Ø 10 mm, 2 mm thick) per modification of Alloy 400 were measured simultaneously to give the average value reported. Prior to the measurements with the laser flash, the thicknesses of the samples were accurately determined (~10^{-3} mm) with a digital caliper. All samples were then coated on both sides with a 4–5 µm graphite layer to increase the absorption of the laser pulse at the rear surface as well as the emissivity of the heat signal for the measurement by the InSb infrared detector on the front face of the sample.

3. Results and Discussion

3.1. Pre-FBR: Inert Gas Atomization, Powder Post-Processing, and Powder Characterization

3.1.1. Atomization Process

In total, three atomizations were carried out to generate a sufficient powder feedstock for subsequent fluidized bed reactor exposure. One of the atomizations is exemplarily illustrated in Figure 2; the current set temperature (orange), the actual temperatures in the closure rod (center of crucible, grey), and the crucible wall (yellow), as well as the oxygen content in the melting chamber (blue, resolution of the sensor: 1 ppm), changed constantly throughout approximately 160 min of heating. At the start of the heating procedure, the

final temperature was set to 1650 °C. For ten minutes, a gas purging and testing cycle was activated. As can be seen from the blue line, the oxygen content fell from ~20,000 ppm to a value of almost 0 ppm during this cycle and remained at this level for the rest of the heating and atomization procedure. It is important to mention that the oxygen level inside the atomization tower was constantly kept at nearly 0 ppm as well. Hence, oxide formation in the liquid state with the alloying elements was prevented. Right after the initializing cycle (green circle), the set temperature rose from 100 °C to 1650 °C after 120 min post-launch. Accordingly, the yellow line indicating the actual temperature inside the crucible wall rose. This line runs linearly as the induction is constantly incorporating heat into the crucible. For the temperature measured in the middle of the crucible (grey line, inside the closure rod), a different slope was observed. For temperatures < 1080 °C (black circle), it rose constantly (left turn), while for temperatures > 1080 °C, it fell constantly (right turn). The reason can be found in the respective melting temperatures of the elements and pre-alloys, with copper as a major ingredient of the alloy and a liquidus of approximately 1080 °C. Pure copper and copper-based pre-alloys passed through the solid–liquid phase transformation here. Hence, the induced energy was only slightly transferred to further heat the system, while a considerable portion acted as a phase converter [43]. With further high-melting elements in the alloy, the slope decreased even further until reaching the desired atomization temperature of 1650 °C (purple circle). Ultimately, when releasing the closure rod after a short holding time, thus initiating the atomization process, the pressure amounted to 9 bar with a gas stream of nearly 180 Nm^3/h, resulting in a melt mass stream of approximately 2.2 kg/min. Consequently, set and actual temperatures fell to room temperature. Atomized powders were then post-processed.

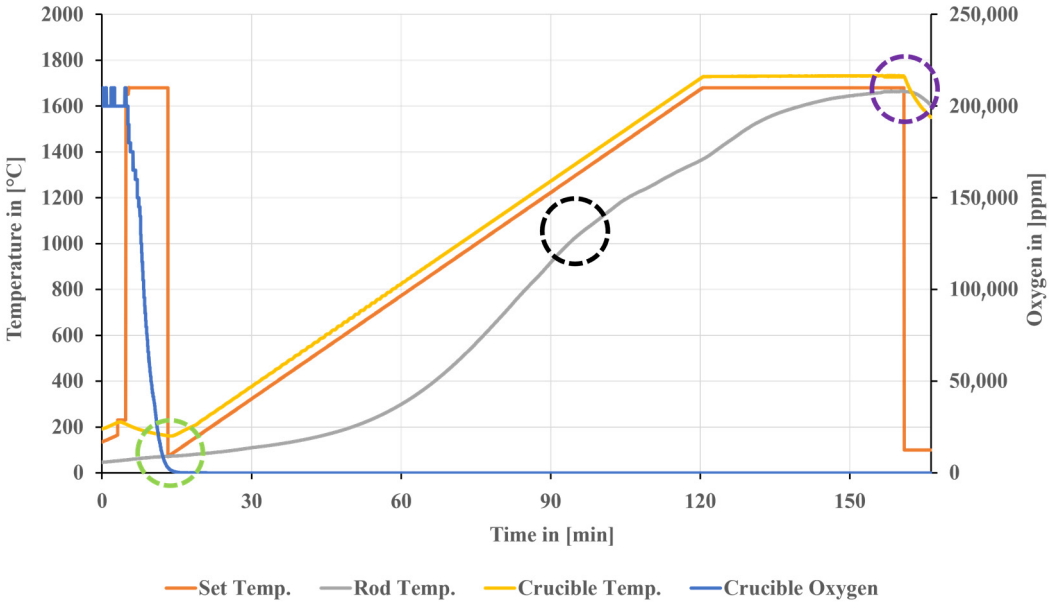

Figure 2. Temperature and oxygen gradients during the pre-atomization heating cycle.

3.1.2. Powder Post-Processing and Pre-FBR Powder Surface Characterization

After cooling down to RT, the powders were post-processed by means of removal of the coarse and fine fractions by sieving and air separation, respectively. The resulting final fraction usable for LPBF revealed both a satisfactory bulk density of ~4.3 g/cm^3 and a flowability of ~14.5 s/50 g. The characteristic particle size distribution was determined as per d_{10} = 21.3 µm, d_{50} = 37.9 µm, and d_{90} = 58.1 µm, fitting very well into the targeted range of 15–63 µm. This way, no particles were too fine or coarse, and thus, restricting LPBF processability was part of the powder feedstock that would be further modified by means of the fluidized bed reactor. Moreover, the sphericity of single particles was determined to be 0.816 on average and only slight satellite formation (Figure 3a), unavoidably occurring

during VIGA, was found but was acceptable for further processing [44,45]. Considerably higher sphericities could be reached via the application of ultrasonic atomization [46]. However, recoatability during PBF-LB/M is still ensured with these powders, and besides, VIGA allows for remarkably higher yields and industrial scalability than other atomization techniques. Remarkably, even though the atomization was performed under an argon atmosphere, and thus nitrogen uptake should have been suppressed, titanium nanoparticles formed on the surface of powders, as can be seen in Figure 3c,d. It is evident that the NPs primarily formed along surface grain boundaries in the interdendritic region (Figure 3b) linked to the segregation behavior of NiCu alloys (Figure 4d,e) [47–49]. Considering (i) the characteristic cuboidal shape and (ii) the results of accompanying Ti-EDS mapping (Figure 3e), the particles formed can be classified as titanium nitrides [9,50–53]. This leads to the assumption that a marginal proportion of nitrogen remained inside the atomizer even though the system was pressured with shielding gas for over ~2.5 h. Due to the very low free energy of formation/high reactivity of titanium and nitrogen, these few ppm N would be sufficient in order to form a remarkable quantity of TiN NPs in these powders per the reaction equation 2 Ti + N_2 → 2 TiN. More precisely, the NP share was determined as per 0.96% in Figure 3c. Even though unexpected, this is assumed to be only beneficial for the further processing of the powders during FBR conditioning. Furthermore, it can be concluded from the EDS mapping that elemental Ti is present all over the particle as well. Hence, most of the Ti is dissolved in the NiCu-based solid solution still and not solely within the TiN. By exposure to the nitrogen stream during FBR, a considerable part of the remaining Ti share in the solid solution can thus act as nuclei for a more pronounced TiN formation and an increase in NP quantity.

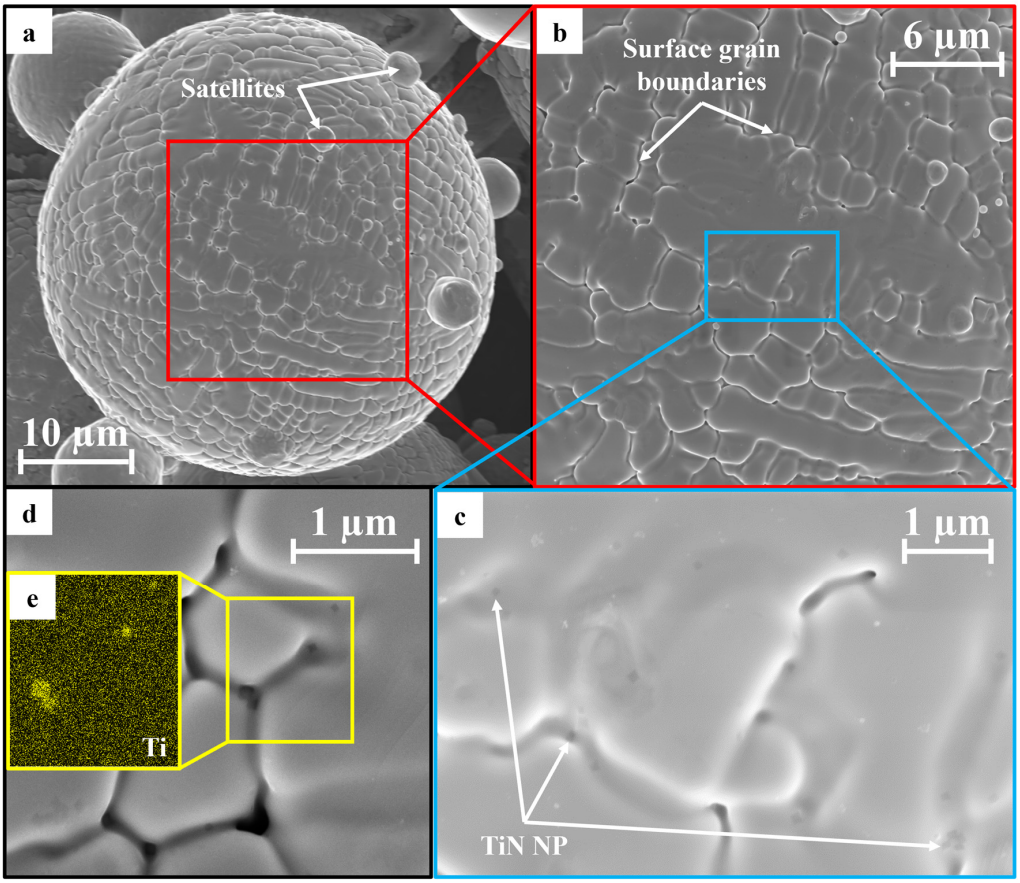

Figure 3. Pre-FBR particle surface SEM characterization revealing (**a**) satellite formation, (**b**) pronounced surface dendrite formation, (**c**) the presence of TiN NPs on GB, (**d**,**e**) a Ti-EDS-mapping on a GB intersection.

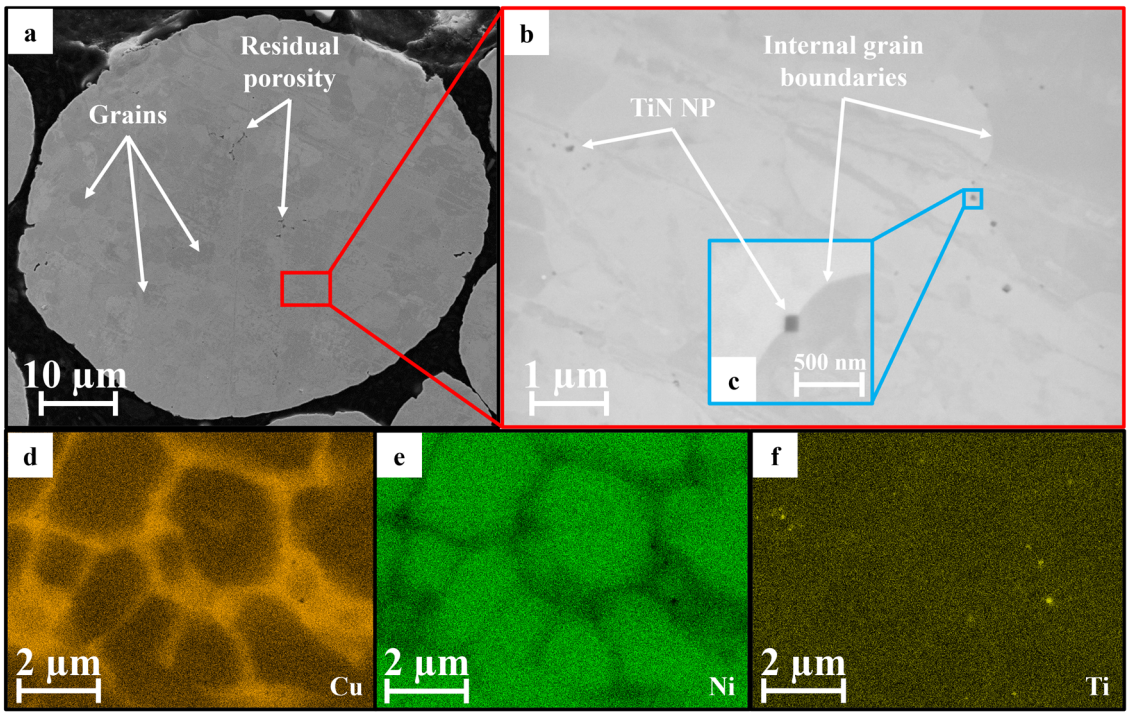

Figure 4. Pre-FBR particle cross-section SEM characterization revealing (**a**) residual porosity, (**b**) the presence of TiN NPs on GB, (**c**) a magnification of a single TiN NP, (**d**–**f**) accompanying Cu-/Ni-/Ti-EDS mappings of (**b**).

3.1.3. Pre-FBR Powder Cross-Section Characterization

From the perspective of achieving a TiN formation on the surface, the assumption arose that TiN would also have formed on the inside of these particles during atomization. By examining the cross section, porosity was detected (see Figure 4a). However, slight residual pore formation is inevitable for gas-atomized metallic powders and is not seen as critically hindering the subsequent LPBF process [54–56]. Equally distributed over the whole cross-section, TiN was detected aligning to internal grain boundaries, representing an NP share of ~0.22% on average (Figure 4b). Thus, from the pre-FBR powder SEM characterization, it can already be concluded that both the surface (pre-FBR ex situ: 0.96%; in situ: 0.12%) and the cross-section (pre-FBR ex situ: 0.22%; in situ: 0.13%) NP concentration is more pronounced than via the GARS approach [9]. At higher magnification (Figure 4c), the characteristic morphology was highlighted in greater detail for a nanoparticle of approx. 100 nm edge length. It can be observed that it is located right in the middle of two colliding grains. The corresponding Cu- and Ni-EDS mappings (Figure 4d,e) provide further information on the well-known Cu segregation phenomenon on grain boundaries of the interdendritic region [47–49]. It can be clearly seen that Cu was predominantly present at GB, while Ni was rather present within the grains. Moreover, both mappings revealed several black dots that corresponded to an increased Ti intensity within the Ti mapping (Figure 4f). Hence, in the same manner that TiN NPs form on surface grain walls, they also form on inner laying grain boundaries of as-atomized powder particles with a maximum detected size of 150 nm edge length. Via STEM characterization on the nanoscale, single NPs were detected on or near the GB as well (Figure 5a). According to both their cuboidal shape and the respective Ti- and N-EDS mappings, the preliminary assumption that the NPs detected via SEM can indeed be classified as TiN was confirmed (Figure 5b,c). These particles revealed a mean diameter of ~50–100 nm, which corresponded to the particle edge length for TiN NPs found in GARS-atomized in situ powders [9]. Further reactants such as Al or O were not found in the same location. The reason for encountering NPs on the surface and inside the powder can be found in the very high cooling rates during atomization; as

the cooling of the melt occurred at a speed of up to 10^4 K/s, solidification occurred nearly instantly throughout the whole particle [57–61]. Therefore, right before the liquid–solid phase transition, encapsulated nitrogen within the particle melt formed TiN to a rather low degree (→0.22%), while the outer side was exposed to a higher level of remaining elemental nitrogen within the argon atmosphere (→0.96%).

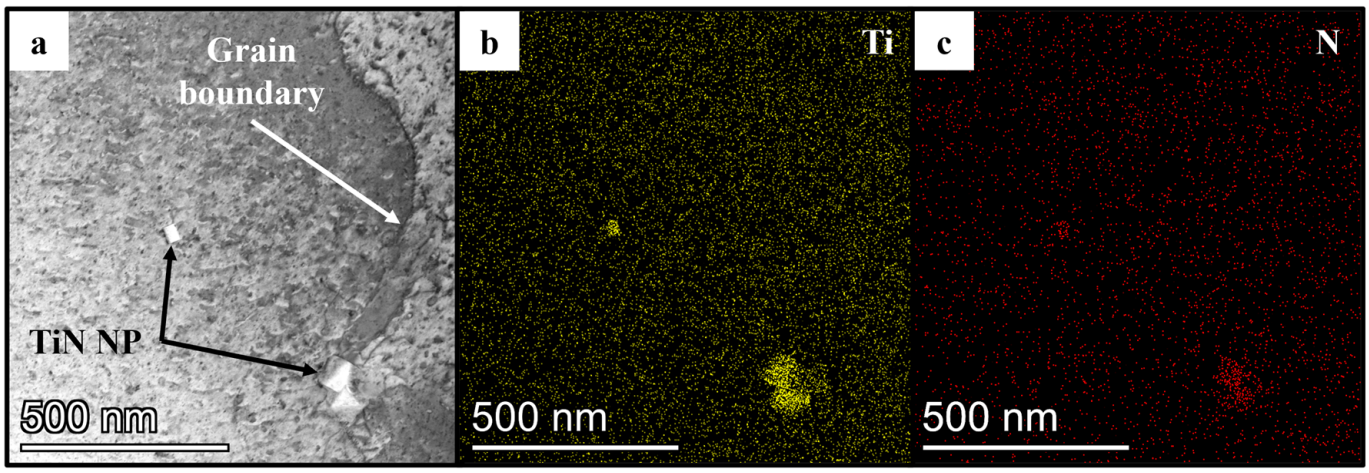

Figure 5. Pre-FBR particle STEM characterization revealing (**a**) magnification of GB area and TiN nanoparticles and (**b**,**c**) accompanying Ti-/N-EDS mappings of (**a**).

3.2. Post-FBR: Fluidized Bed Reactor and Powder Characterization

3.2.1. Post-FBR Powder Surface Characterization

The intermediate powder was further processed via the fluidized bed reactor. Here, a temperature of 800 °C and a constant nitrogen gas flow of 1.2 L/min (4 h) were set as FBR process parameters, as described above. The resulting final powder revealed a bulk density of ~4.7 g/cm^3 and a flowability of ~15.2 s/50 g. Hence, these properties only changed marginally during FBR exposure, not leading to a substantially different behavior during LPBF. The PSD revealed key values of d_{10} = 20.2 µm, d_{50} = 38.8 µm, and d_{90} = 59.8 µm, also being very much in line with the previous powders and within the desired range. Still, a slight difference became apparent when examining the post-FBR particle surface; the grain boundaries were not as pronounced/deep as for the pre-FBR counterpart (Figure 6a). The effect can be traced back to a slight, temperature-induced grain coarsening during FBR, closing these cavities [62,63]. This also serves as an explanation for the slightly higher bulk density, which is beneficial for stable LPBF manufacturing. The TiN formation can be compared to the intermediate state of the powders; NPs primarily formed along surface GB and could barely be found inside grains (Figure 6b,c). The main difference was in the NP quantity as the fraction rose from 0.96% (pre-FBR) by 0.84% to 1.80% (post-FBR) as a result of the exposure to nitrogen during FBR. This also marks a significant increase when compared to the GARS method, which revealed a surface NP fraction of 0.12% only [9]. The NP quantity in the post-FBR powders could be increased by longer exposure during FBR. However, (i) as these 1.80% act as a source for further TiN nucleation within the subsequent additively manufactured parts, thus even further increasing the share, and (ii) since a too high NP quantity leads to both a substantial loss in ductility and sudden fracture mechanism, the current share is considered optimal for further processing.

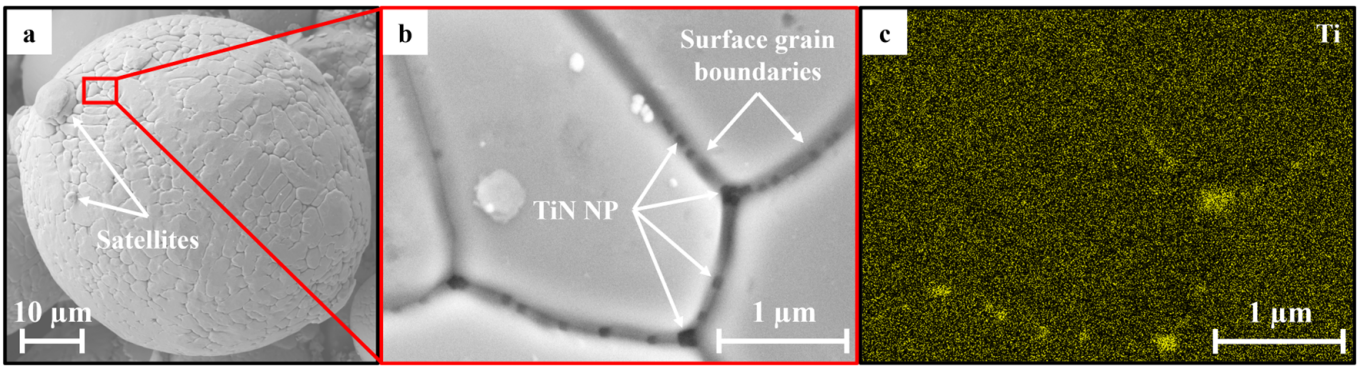

Figure 6. Post-FBR particle surface SEM characterization revealing (**a**) occasional satellite formation, (**b**) the presence of a high quantity of TiN NPs on surface GB, and (**c**) an accompanying Ti-EDS mapping of (**b**).

3.2.2. Post-FBR Powder Cross-Section Characterization

Subsequently, the cross-section of the post-FBR state was further characterized (Figure 7a). In terms of grain evolution and porosity detected, no significant difference was recorded in comparison to the pre-FBR powder (cf. Figure 4). However, the NP fraction increased by 0.66% from 0.22% (pre-FBR) to 0.88% (post-FBR) while revealing a maximum NP size of 150 nm, with the great majority being within 50–100 nm edge length as well (Figure 7b). Also, considering the NP fraction on the cross-section of GARS in situ powders, which amounted to only 0.13%, a clear improvement originating from the FBR processing can be noted [9]. To summarize, also considering the high amount of surface NPs, FBR exposure led to a substantial multiplication of TiN nanoparticles, hence fulfilling the main aim of this work. As the powders remained in the solid state during FBR, the mechanism for nitrogen uptake on the inner side of the particles was a diffusion-controlled one [64]. Over the 4 h exposure, the nitrogen diffused deeper into the particle along grain boundaries, forming TiN with elemental Ti, which detached from the solid solution due to the high temperature applied and its high reactivity with N. As the NP fraction on the surface increased by 0.84% while on the inside, only a 0.66% shift was reported, and the direction of the diffusion mechanism can be clearly traced back to "from outside to inside". Hence, FBR exposure is more effective on the outside of powder particles (=N gas contact area) than on their inside, as expected. Comparing the EDS mappings for Cu, Ni, and Ti in Figure 7c–e, it again becomes apparent that strong Cu segregation on grain boundaries occurred and moreover, that the TiN NPs are located along these GB but almost never within the grains. This was proven to be the case via STEM-EDS as well (Figure 8b–d); most TiN nanoparticles aligned along the magnified GB while occasionally only NPs were detected approximately 150 nm apart from it. Checked against the GARS method and the pre-FBR powders, it becomes apparent that there were not only coarse NPs in the mean size of 50–100 nm but also considerably finer particles, some of which were only 10 nm (cf. Figure 8c) [9]. Hence, in post-FBR powders, the titanium nitride evolution can be described as bimodal [8,65,66]. This is assumed to be beneficial for the Orowan strengthening in parts manufactured using these powders, as there is a contrasting effect of decreasing NP size and more effective strengthening [67,68]. As the coarse NPs were already detected in pre-FBR powders, the additional fine NPs detected in post-FBR powders were considered the direct outcome of the FBR process. Also, dislocation formation occurred near grain boundaries and segregations (Figure 8a). This can be attributed to solid solution segregations eventually leading to the formation of dislocations: as the lattice constants of the Cu-rich segregation area and the neighboring NiCu-rich solid solution varied, interfacial strain was evoked, which, in turn, was circumvented by the formation of dislocations [69].

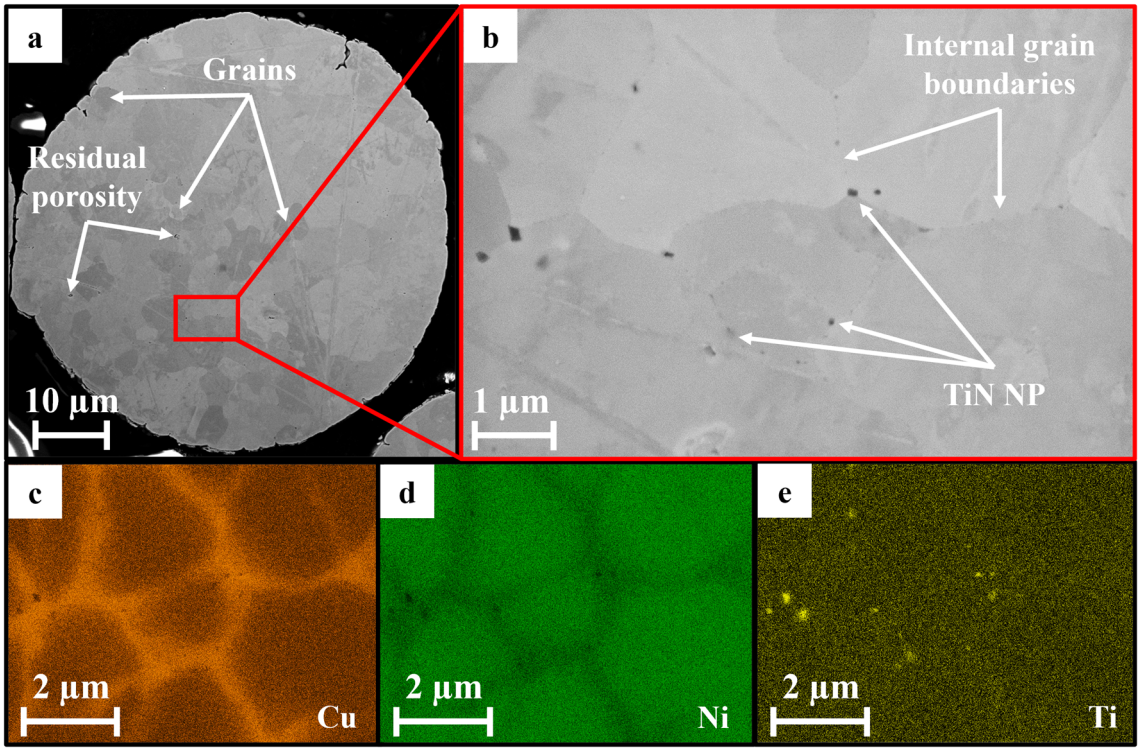

Figure 7. Post-FBR particle cross-section SEM characterization revealing (**a**) occasional porosity, (**b**) the presence of TiN NPs on GB, (**c**–**e**) accompanying Cu-/Ni-/Ti-EDS mappings of (**b**).

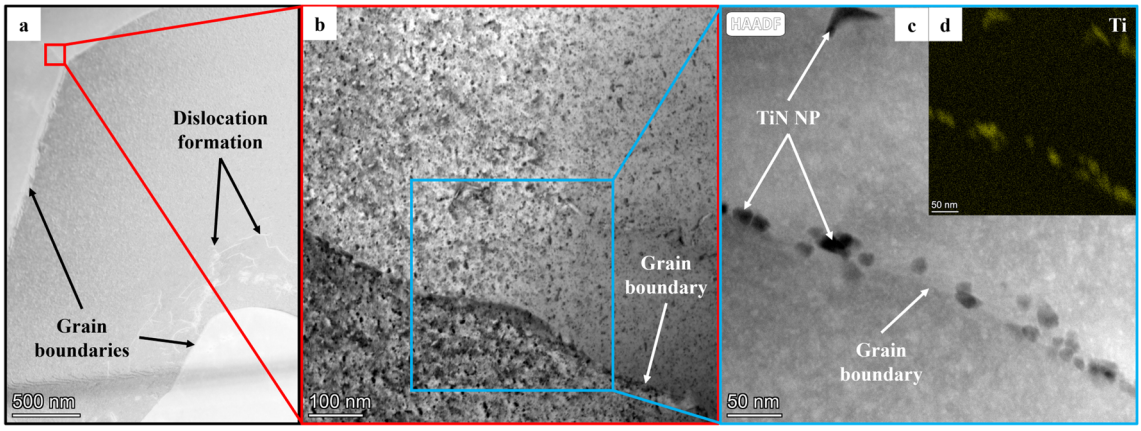

Figure 8. Post-FBR particle STEM characterization revealing (**a**) occasional dislocation accumulation within grains, (**b**) magnification of GB area, (**c**,**d**) dark field and Ti-EDS-mapping of GB rich in TiN nanoparticles.

3.2.3. Powder Cu Segregation and Nanoparticle Formation Mechanism

It is remarkable that nanoparticles in both the pre- and the post-FBR states primarily accumulated along surface and internal grain boundaries rather than inside the respective grains. Also, as discussed, Cu tends to segregate, meaning that the majority of Cu is present along GB, while simultaneously, the larger proportion of Ni can be found within the grains. Still, Alloy 400 forms an fcc solid solution of Cu and Ni [1,2]. Therefore, in order to generate a deeper understanding of the various formation mechanisms occurring during gas atomization and FBR, a sequence of solidification during atomization is proposed in Figure 9, and a mechanism for the increased NP quantity in post-FBR powders is suggested in Figure 10. The first sequence is split up into the four points of time t0 (actual temperature T_0 being higher than the melting temperature of titanium $T_{m,Ti}$), t_1 (T_1 being in between

$T_{m,Ti}$ and the melting temperature of nickel $T_{m,Ni}$), t_2 (T_2 being in between $T_{m,Ni}$ and the melting temperature of copper $T_{m,Cu}$), and t_3 (T_3 being below $T_{m,Cu}$). As nitrogen reveals a boiling point of −196 °C, it is considered gaseous throughout the whole cooling procedure, apart from the portion that forms a compound with titanium as TiN. The remaining N may thus move freely throughout the solid solution fcc structure. At t_0, Ti, Ni, and Cu are in the liquid phase, forming the melt. Hence, no crystal structure is present, and all atoms flow freely. As the temperature drops to T_1 and thus exceeds the Ti solidification temperature, TiN starts forming. Due to the marginal quantity of N in the atomization atmosphere (Ar pressured system), only a small proportion of the Ti added to the alloy would react to TiN. The reason for the segregation behavior can instead be traced back to the significantly different solidification temperatures of Cu (1085 °C) and Ni (1455 °C) [70–72]. As a result, during the solid solution nucleation of the NiCu system (cf. T_2), grain cores, where nucleation originates, experience a higher intensity in Ni than in Cu. Also, the leftover Ti not forming TiN now starts forming part of the solid solution. In between T_2 and T_3, a remarkable portion of Ni is already in the solid state, while the main part of Cu is still in the liquid phase of the melt. Therefore, the Cu-rich melt is being "pushed" by the steadily growing Ni-rich grains until encountering an opposite grain. In the same manner, TiN NPs flow with the melt towards the future GB area. Here, the remaining Cu not enclosed in the grain cores yet would then solidify into the preferred fcc solid solution (T_3). As a result, after complete cooling below the melting temperature of Cu ($T_{m,Cu}$), grain boundary near regions are rich in Cu atoms as part of the solid solution (with Ni and Ti also being present at GB but to a clearly smaller extent). The TiN NPs are now incorporated into the alloy along its grain boundaries. Also, when T_3 is reached, no more melt is present, and the whole alloy system is in the solid state. It is worth mentioning that due to the high cooling rates described previously [57–61], the proposed sequence of Figure 9 takes place extremely fast, and thus, the phase transformation does not take place in an equilibrium state [73–75]. Therefore, the proposed mechanism must be considered a simplified visualization.

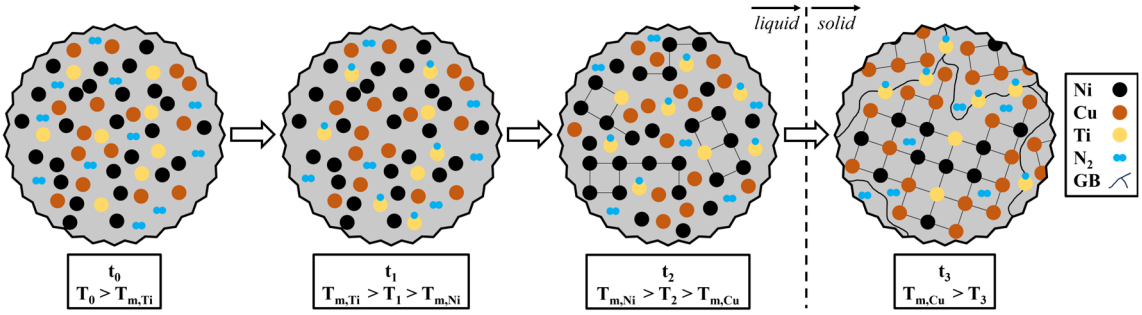

Figure 9. Pre-FBR: a proposed mechanism for the emergence of NP GB accumulation and Cu segregation over time, depending on the liquid–solid phase transition temperatures of the respective elements.

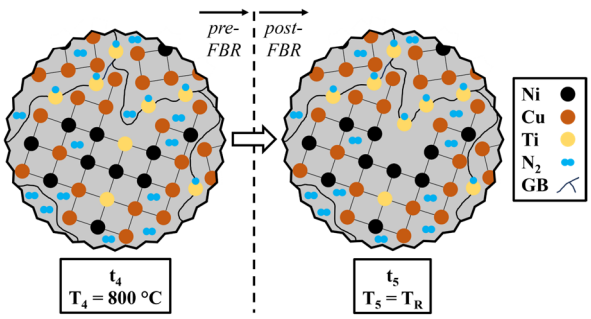

Figure 10. Post-FBR: a proposed mechanism for the increase of TiN NP quantity.

Considering the FBR exposure, a new temperature T_4 is set to 800 °C inside the reactor. As the melting point of Alloy 400 is considerably higher, this process takes place in the solid state only. Hence, the microstructure of t_4 can be compared to the one of t_3, revealing a higher N fraction (cf. Figure 10). As the process is carried out over 4 h at an elevated temperature, a share of the Ti being embedded in the solid solution would now react with the N gas flow. Enabled by diffusion processes, nitrogen is transported along grain boundaries inside the powder, and Ti near these GB leaves its place in the fcc structure to accumulate on the grain boundaries as TiN (cf. t_5, T_R = room temperature). As a result of the FBR process and the low additional surface energy for precipitate formation on GB, the NP fraction is raised, as documented before.

3.3. LPBF Parameter Optimization and Part Characterization

3.3.1. Laser Powder Bed Fusion Optimization

As the intermediate pre-FBR powder (modified in chemical composition, non-modified via FBR yet) already revealed a formation of TiN nanoparticles, its printability and the resulting NP formation in parts were considered. Hence, an LPBF parameter optimization of one iteration, consisting of 24 parameter sets, was carried out in order to gain a deeper understanding of defects occurring during 3D printing and the micro-/nanostructure formation. The parameter sets varied in laser power (7–95 W), scanning speed (100–1150 mm/s), and hatch distance (60–80 µm). Amongst these, 85 W, 1100 mm/s, and 70 µm showed a maximum density of 99.5%, as illustrated in Figure 11 (left). Occasional keyhole defects occurred, especially in the edge areas of the part, being attributed to local beam acceleration and the resulting heat accumulation [76–78]. Porosity is always detrimental to the mechanical properties of the part. Still, small pores below ~50 µm would not result in a massive decline in mechanical performance, as it is rather dependent on microstructural properties [79–81]. The achieved level of 0.5% porosity can thus be accepted while still leaving room for improvement during the final parameter optimization of the FBR-modified alloy, which was split up into two iterations, resulting in 41 parameter combinations. Laser power varied from 35 to 135 W, scanning speed from 700 to 1300 mm/s, and hatch distance from 30 to 70 µm. By applying a parameter set of 115 W, 900 mm/s, and 60 µm, a maximum density of 99.87% could be reached (Figure 11 (right)), again revealing most of the residual porosity in border areas. In contrast to the pre-FBR part, the inner side of the density cube barely showed porosity, which contributes considerably to the density increase of nearly 0.4%. Also, the average size of keyhole porosity was significantly smaller (pre-FBR: ~150 µm, post-FBR: ~70 µm). It is thus assumed that the post-FBR process is better adjusted during all phases of the laser travel (constant speed, acceleration, deacceleration, and turning) [78,82]. The newly found post-FBR parameter set was used for LPBF manufacturing of all test specimens, as presented in the following sections.

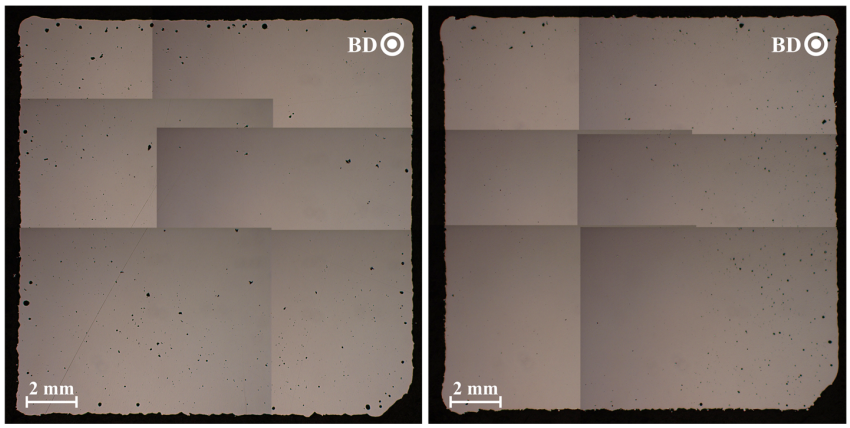

Figure 11. Cross-sections of pre-FBR (**left**) and post-FBR (**right**) density cubes perpendicular to their build directions.

3.3.2. Pre- and Post-FBR Part EBSD Characterization

LPBF-built parts were further analyzed by application of EBSD. The pre-FBR characterization is illustrated in Figure 12, and the post-FBR one in Figure 13. Considering the EBSD mappings (Figures 12a and 13a), a considerable difference becomes present; even though examined under the same magnification, the pre-FBR part revealed a considerably less-ordered grain structure, consisting of a high number of different grain sizes that originated from the respective LPBF process. Thus, besides the previously reported density increase for the post-FBR parts, the grain evolution also occurs more structured, allowing for a smoother LPBF process. The tendency of grains stacking on top of each other and the resulting growth of columns along the build direction, as a function of the directed heat propagation during LPBF, was more apparent [83,84]. Also, the grain diameter was affected, as the post-FBR parts revealed a mean value of 7.44 µm in contrast to 5.20 µm for the pre-FBR ones, while both modifications reveal a max. of ~80 µm in grain size. While small grain sizes in LPBF parts are generally beneficial for mechanical performance according to Hall–Petch, porosity is detrimental [1,40,85–87]. Thus, as the mean grain diameter in post-FBR parts was only ~2 µm coarser than in pre-FBR ones while simultaneously revealing a very high density of ~99.9%, the microstructure in post-FBR parts was favored. Moreover, high dislocation density and low texture are improving mechanical properties, both being the case for the post-FBR state [88,89]. The difference in texture can mainly be correlated with the circumstance that considerably more nanoparticles were present in the post-FBR component than in the pre-FBR one (cf. 3.3.3.). Thus, grain nucleation may occur on these high temperature stable NPs in a controlled manner during the liquid–solid transition, whereas the absence of TiN leads to randomly distributed and directed grains. The lower density mentioned for pre-FBR parts and, thus, the reduced adjustment of process parameters also contributed to this texture formation. Comparing dislocation mappings in both Figures 12b and 13b, the post-FBR material revealed considerably fewer grain boundaries (black) than the pre-FBR one, as no such high number of small-sized grains was present. At once, the post-FBR microstructure revealed a profound dislocation density (green), preferably as geometrically necessary dislocations forming along grain boundaries and to a lesser extent as statistically stored dislocations (SSD) within grain cores [89]. For the pre-FBR version, a GND mean of 4.73 $\times$ 10^{14}/m^2 was detected, which was a significant improvement to the 3.58 $\times$ 10^{14}/m^2 being present in the in situ atomized material [9]. However, the post-FBR material resulted in an even slightly higher GND mean value of 4.86 $\times$ 10^{14}/m^2. Evaluating the respective (inverse) pole figures (IPF/PF) of both modifications (Figures 12c and 13c), several randomly dispersed textures can be stated for the pre-FBR alloy. The {100}, {110}, and {111} PFs did not indicate a clearly preferred texture, while several textures were observed as per the IPF for the build direction X [111] and within the Y/Z layer [101]/[111]. In contrast, the PFs in Figure 13c show a uniform distribution around the [001] center. Moreover, only little texture can be reported throughout the IPF, with a single preference for [001] along X (build direction), revealing a low standardized maximum of 1.79. As reported by Zhao et al. [88], a weakly pronounced texture is beneficial for both an improvement in mechanical properties and a decrease in anisotropy and, thus, desired.

3.3.3. Pre- and Post-FBR Part EDS Characterization

In terms of attainable density, GND, and texture, it can be stated from the above results that the post-FBR alloy (the final state of the applied modification route) revealed a higher potential for improving the properties of the part than the pre-FBR one. However, it has to be clarified whether the nanoparticle share in the final version is also higher than in the intermediate one, and thus, an improved strengthening of a final component can be ensured. Nanostructures of both the pre- and the post-FBR parts were analyzed by utilization of STEM. Figure 14a illustrates the pre-FBR part microstructure. It becomes apparent that, in contrast to the powders, the material is now organized in a micro-dendritic cell nanostructure. Evoked by the very high cooling rates during LPBF of up to 10^6 K/s, such

cell structures and high dislocation formation are frequently documented, particularities for additively manufactured parts, significantly contributing to an enhanced mechanical performance [82,90–94]. Even though hard to detect and to a small extent of only 0.12%, TiN nanoparticles were found throughout the cells, pinning and curving the dislocations (Figure 14 a–c). Such low NP shares in additively manufactured components may already contribute to its performance in a sufficient manner as documented by, e.g., Doñate-Buendia et al. (0.08% Y_2O_3) [66], Smith et al. (0.6% Y_2O_3) [33], and Dai et al. (0.26% Y_2O_3) [30]. However, considerably higher proportions of up to 7.0% are stated as well in the literature, leading to a substantial improvement in mechanical properties [8,30,38,95]. Hence, increasing the strengthening NP share considerably is generally desired. The size of these NPs resulting from shielding gas atomization are in the range of 50–100 nm, as was the case for the pre-FBR powders as well (and for the in situ manufactured parts) [9]. Hence, these NPs can again be described as coarse and monomodal (no finer NPs below 50 nm are present in the pre-FBR state).

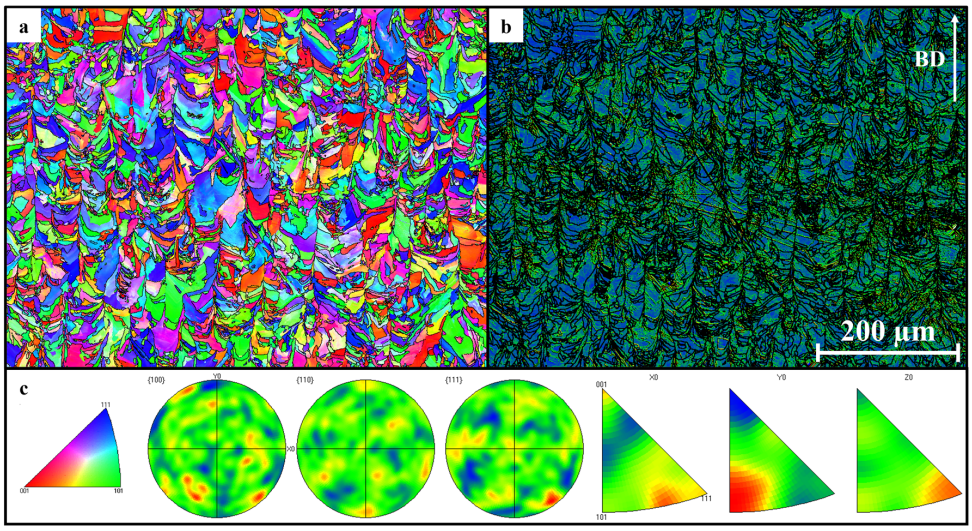

Figure 12. Pre-FBR part EBSD characterization revealing (**a**) X-EBSD mapping in build direction, (**b**) GND distribution map of (**a**), (**c**) color code triangle of (**a**), and resulting pole figures and inverse pole figures for X (=build direction)/Y/Z.

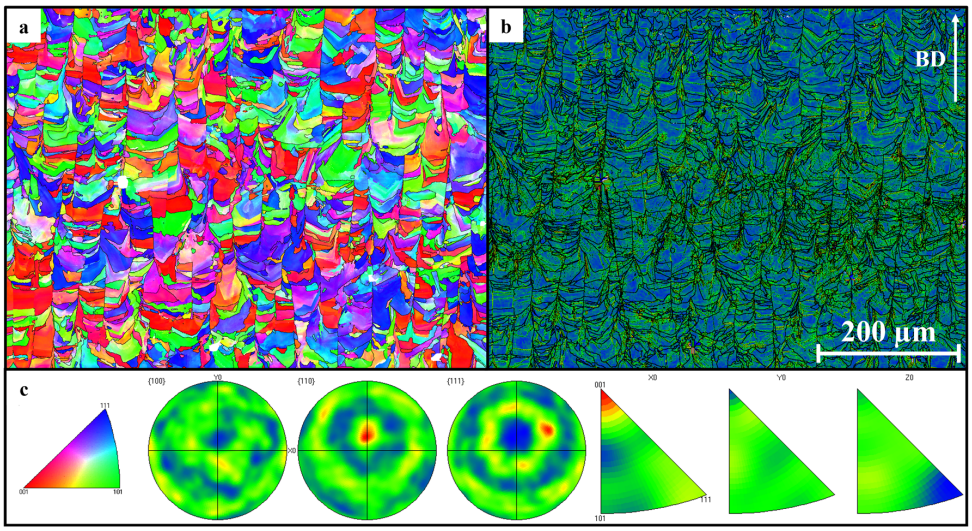

Figure 13. Post-FBR part EBSD characterization revealing (**a**) X-EBSD mapping in build direction, (**b**) GND distribution map of (**a**), (**c**) color code triangle of (**a**), and resulting pole figures and inverse pole figures for X (=build direction)/Y/Z.

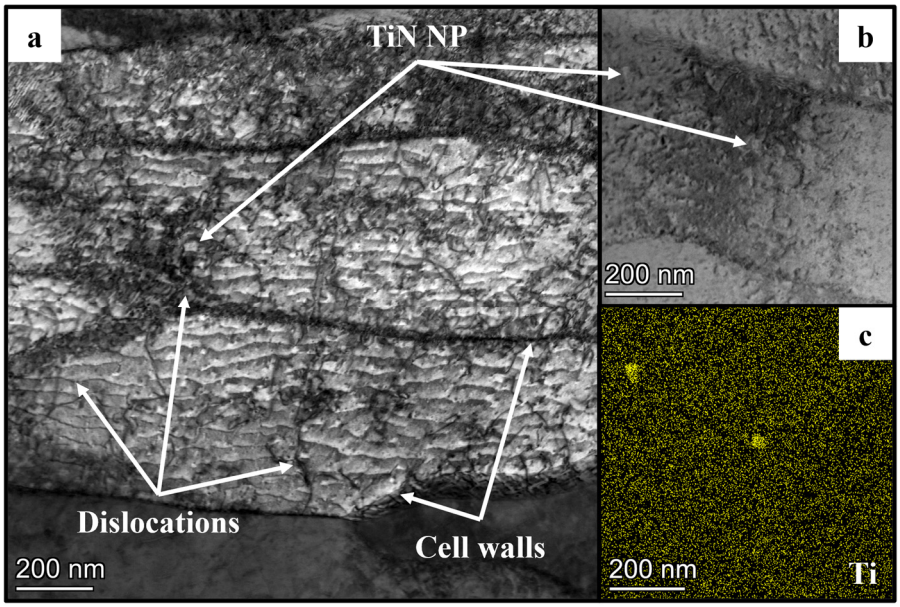

Figure 14. Pre-FBR part STEM-EDS characterization revealing (**a**) a cellular nanostructure, (**b**) occasional presence of TiN NPs, and (**c**) accompanying Ti-EDS mapping of (**b**).

The post-treatment of powders via the fluidized bed reactor increased the NP share in a considerable manner. As displayed in Figure 15a,b, elongated cells were found to be rich in both dislocations and TiN nanoparticles. The NP proportion was 6.53%, which not only represents a significant improvement to the pre-FBR material but also in the in situ processed alloy, which revealed a TiN share of 3.88% only [9]. As mentioned, such proportions are expected to result in enhanced mechanical performance [8,38,95]. A minor portion of NPs can be found within cell cores (i.e., not along their walls), being attached to dislocations, which was also found for the pre-FBR material (Figure 15c,d). However, the great majority of TiN in the post-FBR part primarily aligned along cell walls, as is typical for dispersion-strengthened, LPBF-manufactured components [31,96]. The underlying principle can be explained as per the suggested mechanism for the emergence of NP accumulation in powders (cf. Figure 9), with the difference of accumulation occurring on cell walls instead of grain boundaries because no cell walls were present in the powders. Interestingly, besides plenty of TiN nanoparticles, alumina nanoparticles also formed to a very low extent (Figure 15e,f). They can be clearly differentiated from the cuboidal TiN particles as they appear completely spherical and are not present in the same place. These particles resulted from the reaction $4\ Al + 3\ O_2 \rightarrow 2\ Al_2O_3$ occurring in the melt pool between elemental Al as part of Alloy 400 and the remaining atmospheric oxygen in the shielding gas-pressured LPBF building chamber. As the portion of Al_2O_3 is relatively low, and the precipitates are not spread homogeneously over the microstructure, they are not considered to contribute highly to the dispersion-strengthening effect. However, Figure 15g illustrates the interaction of alumina with dislocations; dislocations are hindered in their expansion by the alumina and bulge around the nanoparticles. This bending effect becomes even more present with the nanosized TiN particles (Figure 15h). The NPs are located at the "upper" end of the dislocations, meaning that they can be considered the origin for cutting the dislocation chain into the many small sections. The size of a single TiN NP is hard to measure but was determined with approx. 10 nm in diameter (as already detected in the post-FBR powders, cf. Figure 8). As in the powders, these fine NPs were not the only manifestation of titanium nitride; there also existed noticeable coarser TiN particles with an average diameter of ~50–100 nm, which is equivalent to a factor of at least 5 times the diameter of the finer particles. However, these coarser particles did not occur frequently throughout the microstructure of the post-FBR parts, but still, a bimodal nanoparticle formation was found [8,65,66]. In Figure 15i, such a particle of 200 nm edge

length is illustrated, and it can be observed that there is a high dislocation accumulation at its edges. As a result, dislocation pinning occurs on both fine and coarse nanoparticles, and thus, both TiN NP types contribute to the dispersion strengthening effect, leading to enhanced mechanical properties.

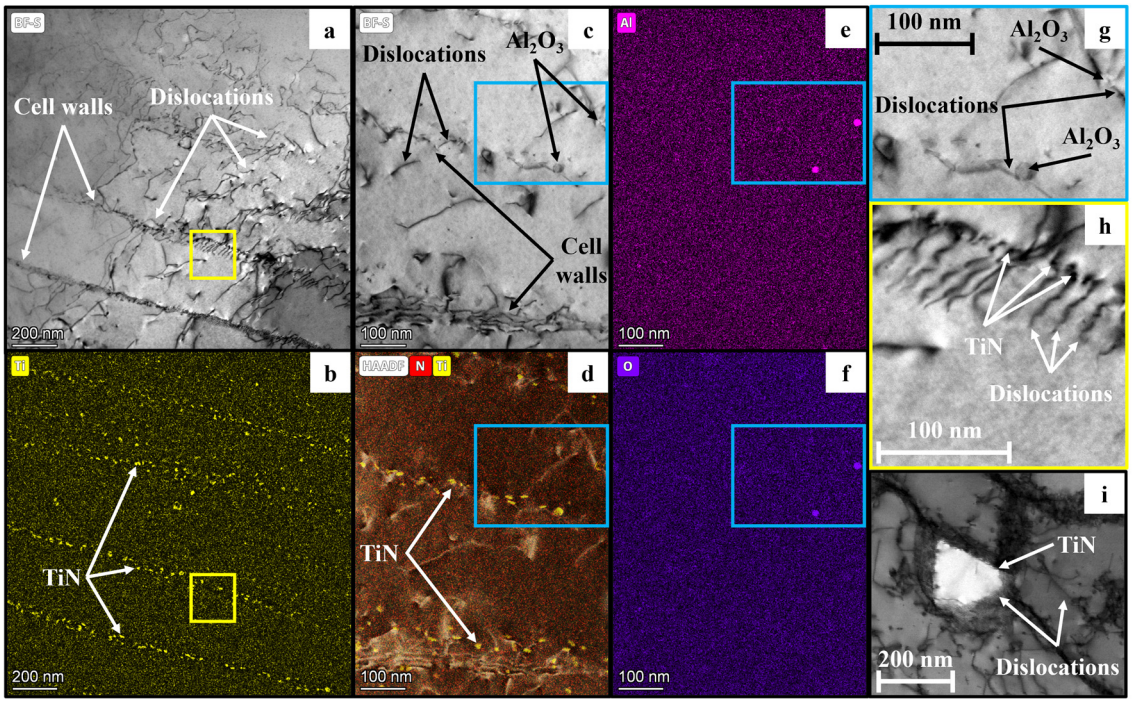

Figure 15. Post-FBR part of STEM-EDS characterization revealing (**a**) a pronounced formation of cell walls and dislocations, (**b**) accompanying Ti-EDS mapping of (**a**), (**c**) a magnified cell wall area, (**d**–**f**) accompanying Ti-N-/Al-/O-EDS mappings of (**c**), (**g**) a magnification of (**c**) illustrating Al_2O_3 dislocation interaction, (**h**) a magnification of (**a**) illustrating TiN dislocation interaction of fine TiN NP, and (**i**) TiN dislocation interaction of a coarse TiN NP.

Pronounced Cu-GB segregation behavior was detected for both the pre-FBR (cf. Figure 4) and the post-FBR (cf. Figure 7) powders. However, such intense chemical splitting of elements Cu on cell walls and Ni within cell cores was not detected for the parts. As per Figure 16a, the micro-dendritic nanostructure described previously became apparent in another form of appearance, not as elongated cells but as smaller spherical and cuboidal cells for a post-FBR part. This was due to the strongly varying solidification direction on the nanoscale; multiple orientations eventually evolved during dynamic melt pool solidification and thus, depending on the area investigated, cells may appear as cellular, elongated, or a mixture of both [92,97]. Considering the accompanying Cu-/Ni-EDS mappings in Figure 16b,c, the Cu segregation behavior of Alloy 400 previously described for the powders (cf. Figure 7c,d) could be redetected in parts as well. However, the intensity of Cu on cell walls was considerably weaker than in powders, and Cu could be detected all over the cells in clear manifestation. Hence, the segregation behavior in LPBF-built parts was highly less-pronounced, which could be correlated with two main differences in comparison to gas atomization. Firstly, the cooling rates were even higher during LPBF than in atomization (up to 10^6 K/s, which equals approximately two orders of magnitude more) [82,90,98]. This led to even less time available for segregation to occur, which is why a high proportion of the elemental Cu was not found solely at cell walls but rather remained inside the homogeneous solid solution during rapid crystallization [99]. In other words, the liquid–solid phase transition of the NiCu system occurred nearly instantly so that the Cu-rich melt was not "pushed" towards the cell walls to such a high extent as was suggested for the GB in powders (cf. Figure 9). Moreover, as already

documented for the gas atomization process, the non-equilibrium solidification behavior during LPBF was even more pronounced [73–75,98–100]. Secondly, the iterative nature of the melting and solidification sequence during LPBF, occurring over several layers, led to the formation of a heat-affected zone [98,101–103]. This zone eventually reduced the segregation manifestation as a heat-induced diffusion was activated, and thus, Cu could reallocate to the solid solution [104–106]. Hence, in summary, when processing Cu segregation-rich powder via LPBF, the considerable decline in segregations in printed parts is dependent on both (i) the high cooling rates, resulting in little time for segregation to occur in the first place, and (ii) the heat affected zone, leading to a further decrease of the already low level of segregations.

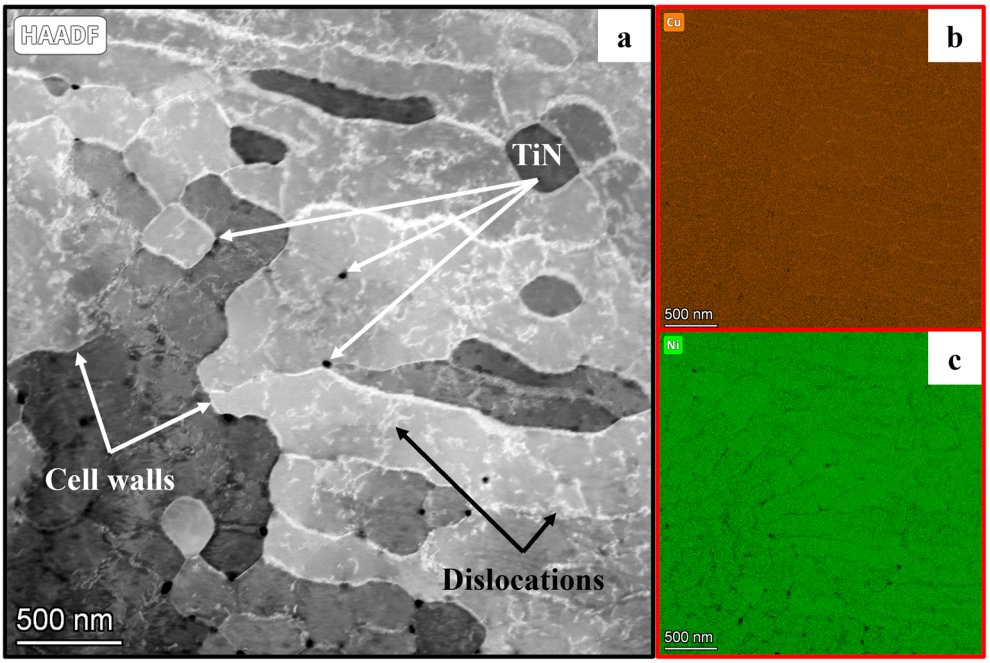

Figure 16. Post-FBR part STEM-EDS characterization revealing (**a**) a pronounced interaction of cell walls, dislocations, and coarse TiN particles and (**b**,**c**) accompanying Cu-/Ni-EDS mapping of (**a**).

3.3.4. Part Melt Pool Formation Mechanism

Based on the microstructural properties of the post-FBR material identified above, an underlying concept for the melt pool formation mechanism was elaborated (Figure 17). Throughout the literature, various approaches for nanoparticle formation throughout the additively manufactured microstructure are demonstrated as a result of an NP-containing powder feedstock or due to reactivity of the melt pool alloying elements with the build chamber atmosphere [10,11,31,33,36]. In this work, a combination of both was the case. As illustrated, the post-FBR powder feedstock was enriched in fine and coarse TiN NPs (cf. Figures 7 and 8). As these powders became molten from the laser and thus experienced a solid–liquid phase transformation, the high-temperature-stable nanoparticles stayed in their original form. However, besides the other alloying elements of Alloy 400, titanium and aluminum atoms from the solid solution of the powders could then flow freely within the melt pool. Especially on the melt pool surface (red highlighted area) as well as within the melt pool, triggered by Marangoni convection [31,36,107], these atoms could then interact with the remaining oxygen and nitrogen of the shielding gas-pressured build chamber. As per $4\ Al + 3\ O_2 \rightarrow 2\ Al_2O_3$ and $2\ Ti + N_2 \rightarrow 2\ TiN$, both molecules, alumina and TiN, began forming. They both deposited on grain boundaries and cell walls during cooling to a columnar microstructure. It is important to mention that alumina was not present in the powders, which is why its formation could be clearly traced back to the LPBF process only. However, TiN was present in the powders already (fine and coarse NPs) and did form

again during LPBF, as the share of fine TiN NPs was significantly increased. This led to the assumption that the TiN formation mechanism can be split up into three stages throughout the whole VIGA-FBR-LPBF process route:

- Primary formation stage:
  Coarse α-TiN resulting from the atomization process (≙ pre-FBR powder state)
- Secondary formation stage:
  Fine β-TiN resulting from the FBR exposure (≙ post-FBR powder state)
- Tertiary formation stage:
  Increase in TiN (=remaining α/β-TiN from powders + γ-TiN formation within melt pool) resulting from the LPBF process (≙ post-FBR part state)

Still, even though three formation stages were introduced, the nature of TiN within the post-FBR material can be characterized as bimodal (the distinction between fine and coarse particles). For the Al_2O_3 formation mechanism, only one stage can be denoted:

- Primary formation stage:
  Comparably coarse α-Al_2O_3 resulting from the LPBF process (≙ post-FBR part state)

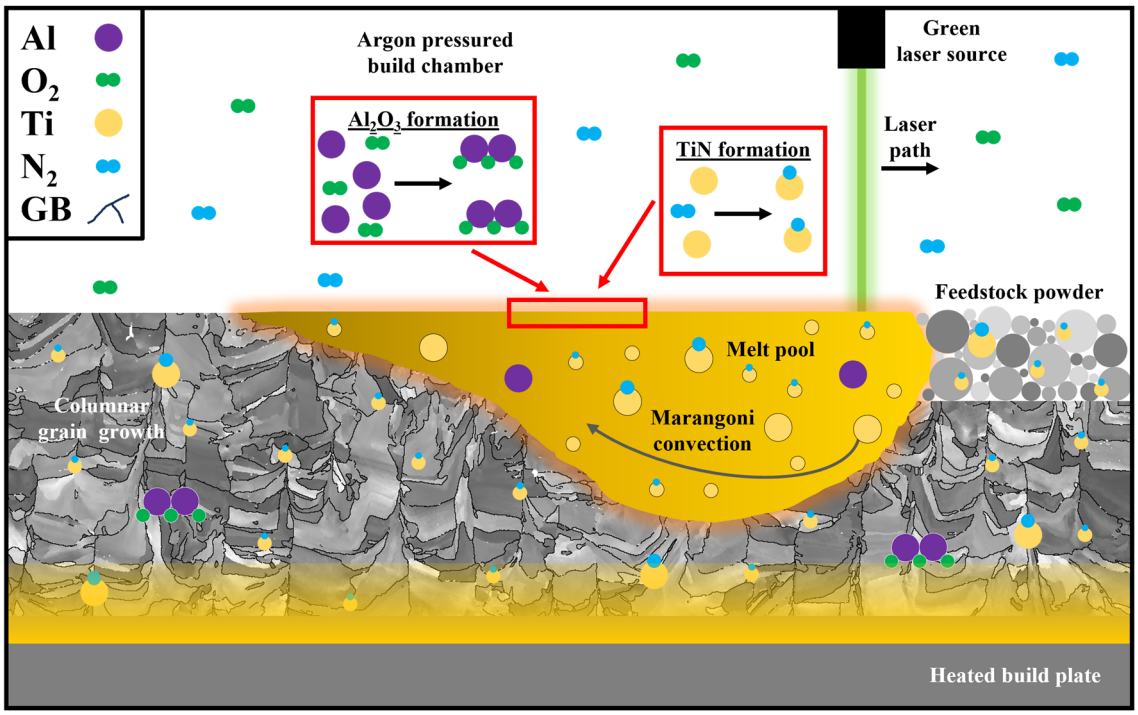

Figure 17. Proposed mechanism for melt pool interaction and microstructure formation during LPBF.

As documented by the EBSD mapping (cf. Figure 13) as well as visualized by STEM characterization (cf. Figures 15 and 16), multiple orientations of single grains exist throughout the microstructure. As a result, the appearance of single cells within a respective grain varies strongly from the cells of another grain (Figure 18); grains I. and III. revealed round cells, while grains II. and IV. showed elongated cells (Figure 18a). The difference in orientation can be further studied for the highlighted area (Figure 18b) and the underlying cell formations (Figure 18c). Cell walls rich in dislocations are present for both grains III. and IV. However, it seems like grain III. revealed significantly more dislocations (see green circle). The reason is that dislocations primarily accumulate along cell walls, as discussed before. Hence, with the orientation of cells present in grain IV. and the resulting lower amount of cell walls visible in this cross-section, the number of dislocations visible was lower as well (see purple circle). Dislocations could be found within cells as well but to a much lower extent, which was due to segregations on cell walls being beneficial for dislocation

formation, as stated for powder grain boundaries before [69]. However, it needs to be addressed that during STEM, the grain boundary and cell wall visibility conditions (g.b, where g is the diffraction vector and b is the Burgers vector) must be met. Thus, reduced visibility of dislocations is influenced by the diffraction pattern and not solely dependent on grain orientations. Still, it can be concluded that the number of dislocations is homogenous throughout the nanostructure and only appears to be heterogeneous due to the steadily varying cell growth directions from one grain to another.

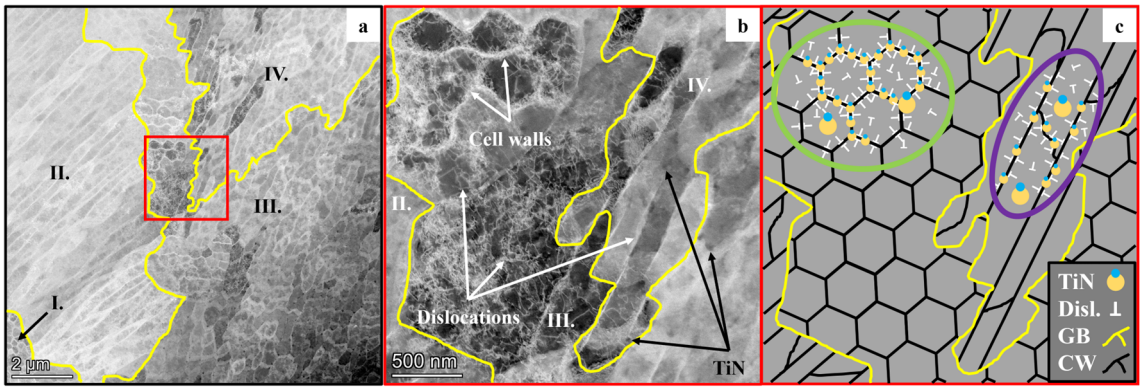

Figure 18. Post-FBR part STEM characterization indicating (**a**) grain formation and underlying cellular structure, (**b**) a magnification of (**a**) highlighting pronounced cell wall–dislocation interaction, and (**c**) corresponding proposed mechanism for nanostructure formation during LPBF as per (**b**).

3.4. Post-FBR Testing

As the pre-FBR powder and part characterization revealed (i) a lower maximum attainable density, (ii) a lower presence of strengthening NPs, (iii) a lower dislocation density, and (iv) a more pronounced texture than the post-FBR ones, only the final state of this modification route, the post-FBR ex situ alloy, was further investigated during mechanical testing. Here, a direct comparison to the GARS in situ processed material [9] was drawn in order to quantify specific drawbacks and improvements achieved via the newly developed FBR processing routine.

3.4.1. Hardness and Tensile Testing

In terms of hardness, the post-FBR nitridation approach led to a mean value of 202 HV10. The nitridation gas atomization reaction synthesis procedure instead enabled the production of parts revealing a slightly higher hardness of 207 HV10 on average. This difference of ~5 HV10 can be accepted if further mechanical properties show an improvement for the FBR material. This was the case for the tensile properties; σ and ε were enhanced in comparison to the in situ version (Figure 19 (left)). As can be seen, the ultimate tensile strength for the post-FBR material was comparable to the GARS material for RT and 400 °C. However, at higher temperatures, the new alloy performed slightly better. A clear improvement compared to unmodified LPBF-processed Alloy 400 became apparent as well. These conclusions also applied to the yield strength. Elongation and contraction from RT to 750 °C are displayed in Figure 19 (right). At the breaking point, the ex situ material revealed the highest elongation for all elevated temperatures of potential application. Again, a considerable advantage over the unmodified version can be stated. Therefore, among the three different material states, FBR conditioning allowed for a superior alloy system in terms of both strength and elongation. The contraction revealed a varying behavior for the modified versions and the unmodified one; at RT and 400 °C, both modified alloys showed a comparably high contraction, but the unmodified did not. From 550 °C on, they all revealed marginal contraction only. Hence, a ductile to brittle transition for the modified parts in the region of 400 °C can be stated, while the unmodified LPBF geometry showed a rather brittle failure mode throughout the whole temperature range tested. The change of failure

mechanism from ductile to brittle can be correlated with decreasing grain size, which is also seen in NiCu alloys at elevated temperatures [72,108]. However, the mean grain diameters did not vary significantly, which is why an effect of the dislocations must be considered. Indeed, the higher the dislocation density, the harder it gets for a single dislocation to move freely throughout the nanostructure, which ultimately causes an increase in strength and a decrease in the ductility of the material [109–111]. Hence, a pronounced dislocation density is the reason for brittle material failure, especially at elevated temperatures up to 750 °C, where increased movement activity is present. Furthermore, the brittle behavior of the unmodified material even at RT is rather caused by a higher level of porosity in contrast to the modified material. Voids and near-grain boundary oxides may cause such brittle failure initiation [37,112]. Figure 20 provides an overview of the exact sequence of the tensile tests for the post-FBR material. The maximum reached UTS that attained elongation at a break for all five temperatures applied can be determined as per:

- RT: 624.4 MPa and 22.5%
- 400 °C: 577.2 MPa and 20.7%
- 550 °C: 457.4 MPa and 13.1%
- 650 °C: 321.8 MPa and 4.5%
- 750 °C: 237.4 MPa and 4.0%

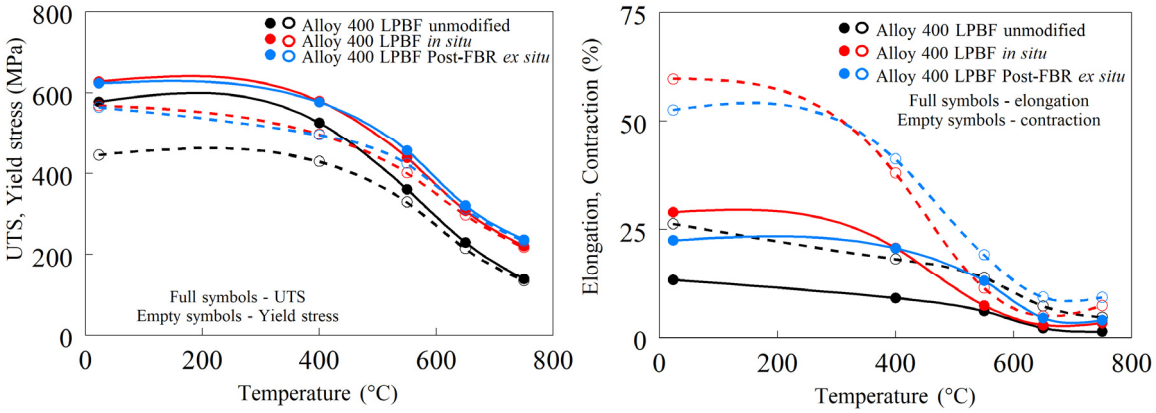

Figure 19. Tensile properties of unmodified reference material, in situ GARS-processed material, and ex situ FBR-processed material.

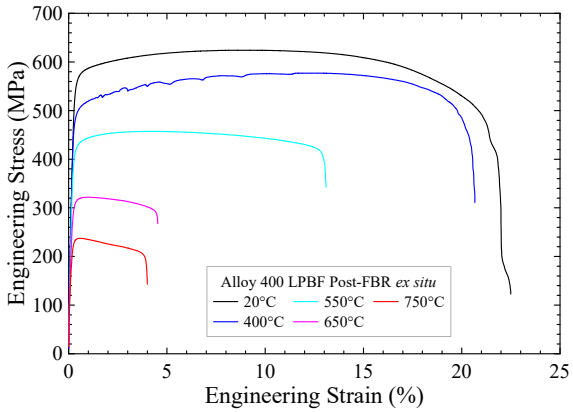

Figure 20. Stress vs. strain diagram of ex situ FBR processed material in the temperature range of RT—750 °C.

A clear positive shift in tensile properties can thus be denoted for the ex situ modification, especially at higher temperatures, where the offset in UTS to unmodified material is more pronounced than at lower temperatures.

3.4.2. Creep and Fatigue Testing

Creep and fatigue experiments were carried out at 650 °C as a potential application temperature of the alloy system. Checked against unmodified and in situ material, Figure 21 (left) illustrates the creep properties of the ex situ alloy in time to rupture t_r for several σ stresses applied. A precise comparison was made for 50, 75, and 100 MPa, and a definite hierarchy became apparent: the newly developed post-FBR material exhibited clearly superior creep properties to the GARS test specimens and the unmodified ones. For instance, at 75 MPa, the ex situ modification endured ~300 h during creep testing, whereas the in situ one failed after ~85 h, with the standard material even breaking at a very low tr of just 8 h. Thus, the TiN dispersion strengthening effect caused an increase of several orders of magnitude, being linked to the dislocation pinning on nanoparticles [26]. Moreover, not only the values achieved were higher but also the gradients of the connecting lines were flatter, meaning that at higher stresses, the modified materials performed even better than with lower stresses anyway. Ultimately, even though the ex situ modification possessed small grain sizes, which were also linked to multiple grain nucleation on the TiN present in the melt pool, the strengthening achieved via these nanoparticles equaled the creep strengthening loss due to grain refinement [27,68,95]. For the same applied temperature of 650 °C, Figure 21 (right) displays the fatigue results in endured number of cycles N_f for several applied stresses σ_a. At first glance, the gradation from ex situ to in situ to unmodified LPBF material can be noted. As the modified versions performed better, a comparison could only be carried out at stresses of 150 and 175 MPa. At the higher stress level, the standard variant of the material did not even reach 2000 cycles. The GARS modification instead showed good fatigue properties of 80,000 cycles until failure, which marks a tremendous advancement already. However, the material designed by FBR throughout this study reached nearly 600,000 cycles. Therefore, similar to creep results, the post-FBR ex situ material showed excellent fatigue properties, not only outperforming the unmodified variant (300x improvement) but also the GARS one (7.5x improvement) due to nanoparticle presence on cell walls [31,113]. In conclusion, considering tensile, creep, and fatigue properties, the newly generated post-FBR ex situ modification marks a significant advancement in the material development of Alloy 400. The reason for the post-FBR material performing clearly better in terms of fatigue and creep during tensile testing, only revealing a slight improvement in comparison to the other two versions, is mainly due to the Orowan mechanism. The pinning of dislocations along the nanoparticles is much more pronounced during the long-term experiments of fatigue and creep. Tensile testing, in turn, occurs instantly, leaving significantly less space for a pronounced dispersoid–dislocation interaction (e.g., pinning of dislocations). This effect even intensifies with rising temperatures [7,31–35].

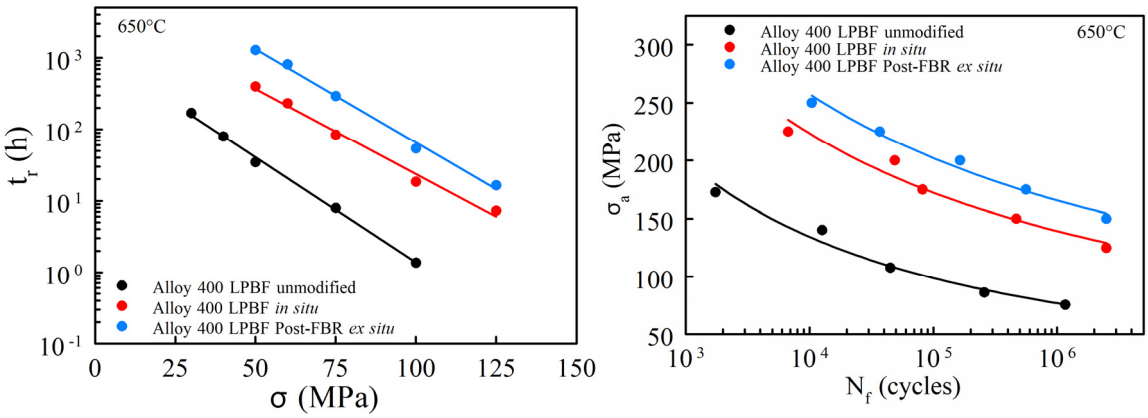

Figure 21. Creep (**left**) and fatigue (**right**) properties of unmodified reference, in situ GARS, and ex situ FBR material.

3.4.3. Thermal Diffusivity

The thermal diffusivity results given in Figure 22 draw a comparison between the different LPBF modifications of Alloy 400 throughout the whole temperature range. They show a clear trend of an increased thermal diffusivity with rising temperature [114]. While there is nearly no difference at low temperatures, a slight difference is observed for the slope of the "Alloy 400 LPBF unmodified" from 300 °C on. The difference is only marginal and can be correlated to the absence of nanoparticles. Apart from that, there are no significant deviations. This indicates that the FBR modification of powders, and thus, the final formation of nanoparticles on cell walls of parts, did not substantially alter the heat transport properties of the material in comparison to unmodified LPBF material (this conclusion is similar for the GARS routine). The results are considered a desirable outcome, as the mechanical properties were successfully improved, as shown previously, while simultaneously, a drawback in heat propagation was avoided, as required for heat exchangers as a potential final application [114–116].

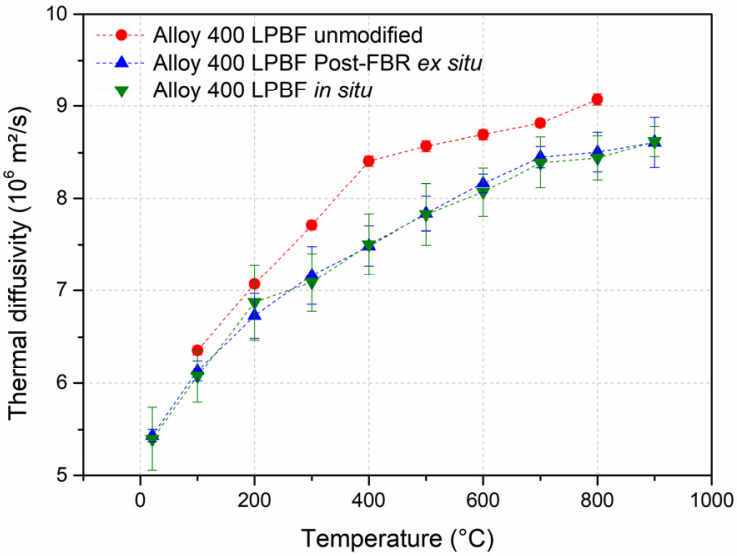

Figure 22. Thermal diffusivity for various modifications of Alloy 400 over temperature.

4. Conclusions

This work elaborated a new approach for a dispersion-strengthened Alloy 400 material system. Processing of shielding gas atomized powders in a fluidized bed reactor, where the particles were set to a nitrogen stream over time and temperature, resulted in a TiN-enriched powder feedstock for LPBF. In-depth characterization at both the micro- and nanoscale was carried out for both powders and parts resulting from this conditioning method, split up into a pre-FBR and a post-FBR fraction. This enabled specific improvements that resulted directly from the fluidized bed reactor process. Formation mechanisms for nanoparticle nucleation, segregation behavior, and cellular evolution of the nanostructure during melt pool solidification were provided and accompanied by mechanical testing of the components produced. Throughout the whole study, specific peculiarities of this ex situ approach were elaborated and set in comparison to the previously introduced in situ GARS variant [9]. Altogether, Table 2 summarizes the pre- and post-FBR results of this work and sets them in relation with the in situ material.

Table 2. Comparison between both process routes, the GARS in situ and the FBR ex situ nitridation approach for Alloy 400.

	In Situ Nitridation [9]	**Pre-FBR Ex Situ Nitridation [This Work, Sections 3.1 and 3.3]**	**Post-FBR Ex Situ Nitridation [This Work, Sections 3.2–3.4]**
Atomization type	GARS (nitrogen) CCA	Shielding gas (argon) CCA	-
Post treatment	-	-	FBR (nitrogen)
Targeted NP in powder	TiN	None	TiN
Detected NP in powder	TiN	TiN	TiN
Appearance form	Monomodal	Monomodal	Bimodal
Powder-TiN-NP diameter in [nm]	Fine: - Coarse: ~50–100	Fine: - Coarse: ~50–100	Fine: ~10 Coarse: ~50–100
NP share in powder in [%]	Surface: 0.12 Inside: 0.13	Surface: 0.96 Inside: 0.22	Surface: 1.80 Inside: 0.88
Bulk density in [g/cm^3]	4.62	4.3	4.7
Flowability in [s/50 g]	14.0	14.5	15.2
Particle size distribution in [d_{10}/d_{50}/d_{90}; µm]	17.3/30.7/51.5	21.3/37.9/58.1	20.2/38.8/59.8
Targeted NP in LPBF part	TiN	None	TiN
Detected NP in LPBF part	TiN, Al_2O_3	TiN, Al_2O_3	TiN, Al_2O_3
Appearance form	Monomodal	Monomodal	Bimodal
Part-TiN-NP diameter in [nm]	Fine: - Coarse: ~50–100	Fine: - Coarse: ~50–100	Fine: ~10 Coarse: ~50–100
NP share in part in [%]	3.88	0.12	6.53
Mean grain diameter in [µm]	6.78	5.20	7.44
GND density in [10^{14}/m^2]	3.58	4.73	4.86
Hardness in [HV10]	207.4	178.8	202.0
Tensile properties	Enhanced σ and ε to unmodified material	-	Enhanced σ and ε to in situ version
Creep properties	Longer t_R to unmodified material	-	Longer t_R to in situ version
Fatigue properties	Higher N_f to unmodified material	-	Higher N_f to in situ version
Thermal diffusivity	≙ ex situ	-	≙ in situ

Ultimately, and in accordance with the above-listed results, it can be concluded that a new, superior Alloy 400 system was generated via the application of the fluidized bed reactor.

Author Contributions: Conceptualization, J.-P.R., U.K. and K.J.; methodology, J.-P.R.; software, J.-P.R., I.Š. and M.G.; validation, J.-P.R.; formal analysis, J.-P.R. and G.B.; investigation, J.-P.R., I.Š., M.G., A.D. and G.B.; resources, F.P., U.K. and K.J.; data curation, J.-P.R., I.Š., M.G., A.D. and G.B.; writing—original draft preparation, J.-P.R.; writing—review and editing, J.-P.R., I.Š., F.P., U.K. and K.J.; visualization, J.-P.R., I.Š., M.G. and G.B.; supervision, J.-P.R., I.Š., G.B., F.P., U.K. and K.J.; project administration, F.P., U.K. and K.J.; funding acquisition, F.P., U.K. and K.J. All authors have read and agreed to the published version of the manuscript.

Funding: This research was funded by the European Union's Horizon 2020 research and innovation program, grant number 958192.

Data Availability Statement: Dataset available on request from the authors.

Acknowledgments: The authors would like to acknowledge QuesTek Europe AB for providing the Ti-modified alloy composition.

Conflicts of Interest: The authors declare no conflicts of interest. The funders had no role in the design of the study; in the collection, analyses, or interpretation of data; in the writing of the manuscript; or in the decision to publish the results.

References

1. Raffeis, I.; Adjei-Kyeremeh, F.; Vroomen, U.; Westhoff, E.; Bremen, S.; Hohoi, A.; Bührig-Polaczek, A. Qualification of a Ni–Cu Alloy for the Laser Powder Bed Fusion Process (LPBF): Its Microstructure and Mechanical Properties. *Appl. Sci.* **2020**, *10*, 3401. [CrossRef]
2. Shoemaker, L.E.; Smith, G.D. A century of monel metal: 1906–2006. *JOM* **2006**, *58*, 22–26. [CrossRef]
3. Special Metals Corporation. High-Performance Alloys for Resistance to Aqueous Corrosion 2000. Available online: https://www.specialmetals.com/documents/aqueous-corrosion-handbook.pdf (accessed on 18 August 2024).
4. Dutta, R.S. Corrosion aspects of Ni–Cr–Fe based and Ni–Cu based steam generator tube materials. *J. Nucl. Mater.* **2009**, *393*, 343–349. [CrossRef]
5. Küçük, Y.; Döleker, K.M.; Gök, M.S.; Dal, S.; Altınay, Y.; Erdoğan, A. Microstructure, hardness and high temperature wear characteristics of boronized Monel 400. *Surf. Coat. Technol.* **2022**, *436*, 128277. [CrossRef]
6. Jahns, K.; Ulrich, A.S.; Schlereth, C.; Reiff, L.; Krupp, U.; Galetz, M.C. The Effect of Cu Content and Surface Finish on the Metal Dusting Resistance of Additively Manufactured NiCu Alloys. *Oxid. Met.* **2021**, *96*, 241–256. [CrossRef]
7. Martin, J.H.; Yahata, B.D.; Hundley, J.M.; Mayer, J.A.; Schaedler, T.A.; Pollock, T.M. 3D printing of high-strength aluminium alloys. *Nature* **2017**, *549*, 365–369. [CrossRef]
8. Ma, S.; Shang, Z.; Shang, A.; Zhang, P.; Tang, C.; Huang, Y.; Leung, C.L.A.; Lee, P.D.; Zhang, X.; Wang, X. Additive manufacturing enabled synergetic strengthening of bimodal reinforcing particles for aluminum matrix composites. *Addit. Manuf.* **2023**, *70*, 103543. [CrossRef]
9. Roth, J.-P.; Šulák, I.; Chlup, Z.; Fischer-Bühner, J.; Krupp, U.; Jahns, K. The dispersion-strengthening effect of TiN evoked by in situ nitridation of NiCu-based Alloy 400 during gas atomization for laser powder bed fusion. *Mater. Sci. Eng. A* **2024**, *893*, 146129. [CrossRef]
10. Horn, T.; Rock, C.; Kaoumi, D.; Anderson, I.; White, E.; Prost, T.; Rieken, J.; Saptarshi, S.; Schoell, R.; DeJong, M.; et al. Laser powder bed fusion additive manufacturing of oxide dispersion strengthened steel using gas atomized reaction synthesis powder. *Mater. Des.* **2022**, *216*, 110574. [CrossRef]
11. Saptarshi, S.; deJong, M.; Rock, C.; Anderson, I.; Napolitano, R.; Forrester, J.; Lapidus, S.; Kaoumi, D.; Horn, T. Laser Powder Bed Fusion of ODS 14YWT from Gas Atomization Reaction Synthesis Precursor Powders. *JOM* **2022**, *74*, 3303–3315. [CrossRef]
12. Zhang, D.; Darsell, J.T.; Wang, J.; Ma, X.; Grant, G.J.; Anderson, I.E.; Rieken, J.R.; Edwards, D.J.; Setyawan, W.; Horn, T.J.; et al. No ball milling needed: Alternative ODS steel manufacturing with gas atomization reaction synthesis (GARS) and friction-based processing. *J. Nucl. Mater.* **2022**, *566*, 153768. [CrossRef]
13. Anderson, I.E.; Foley, J.C. Determining the role of surfaces and interfaces in the powder metallurgy processing of aluminum alloy powders. *Surf. Interface Anal.* **2001**, *31*, 599–608. [CrossRef]
14. Pereira, T.; Kennedy, J.V.; Potgieter, J. A comparison of traditional manufacturing vs additive manufacturing, the best method for the job. *Procedia Manuf.* **2019**, *30*, 11–18. [CrossRef]
15. Pérez, M.; Carou, D.; Rubio, E.M.; Teti, R. Current advances in additive manufacturing. *Procedia CIRP* **2020**, *88*, 439–444. [CrossRef]
16. Gibson, I.; Rosen, D.W.; Stucker, B. (Eds.) *Additive Manufacturing Technologies: 3D Printing, Rapid Prototyping, and Direct Digital Manufacturing*; Springer: New York, NY, USA, 2016; ISBN 978-3-030-56127-7.
17. Guth, S.; Babinský, T.; Antusch, S.; Klein, A.; Kuntz, D.; Šulák, I. Creep–Fatigue Interaction of Inconel 718 Manufactured by Electron Beam Melting. *Adv. Eng. Mater.* **2023**, *25*, 2300294. [CrossRef]
18. Šulák, I.; Babinský, T.; Chlupová, A.; Milovanović, A.; Náhlík, L. Effect of building direction and heat treatment on mechanical properties of Inconel 939 prepared by additive manufacturing. *J. Mech. Sci. Technol.* **2023**, *37*, 1071–1076. [CrossRef]
19. Handal, R. An implementation framework for additive manufacturing in supply chains. *JOSCM* **2017**, *10*, 18–31. [CrossRef]
20. Hopkinson, N.; Dicknes, P. Analysis of rapid manufacturing—Using layer manufacturing processes for production. *Proc. Inst. Mech. Eng. Part C J. Mech. Eng. Sci.* **2003**, *217*, 31–39. [CrossRef]
21. Safaei, K.; Abedi, H.; Nematollahi, M.; Kordizadeh, F.; Dabbaghi, H.; Bayati, P.; Javanbakht, R.; Jahadakbar, A.; Elahinia, M.; Poorganji, B. Additive Manufacturing of NiTi Shape Memory Alloy for Biomedical Applications: Review of the LPBF Process Ecosystem. *JOM* **2021**, *73*, 3771–3786. [CrossRef]
22. Cao, L.; Li, J.; Hu, J.; Liu, H.; Wu, Y.; Zhou, Q. Optimization of surface roughness and dimensional accuracy in LPBF additive manufacturing. *Opt. Laser Technol.* **2021**, *142*, 107246. [CrossRef]
23. Sanchez, S.; Smith, P.; Xu, Z.; Gaspard, G.; Hyde, C.J.; Wits, W.W.; Ashcroft, I.A.; Chen, H.; Clare, A.T. Powder Bed Fusion of nickel-based superalloys: A review. *Int. J. Mach. Tools Manuf.* **2021**, *165*, 103729. [CrossRef]

24. Tian, Z.; Zhang, C.; Wang, D.; Liu, W.; Fang, X.; Wellmann, D.; Zhao, Y.; Tian, Y. A Review on Laser Powder Bed Fusion of Inconel 625 Nickel-Based Alloy. *Appl. Sci.* **2020**, *10*, 81. [CrossRef]
25. Pollock, T.M.; Clarke, A.J.; Babu, S.S. Design and Tailoring of Alloys for Additive Manufacturing. *Met. Mater. Trans. A* **2020**, *51*, 6000–6019. [CrossRef]
26. Boes, J.; Röttger, A.; Becker, L.; Theisen, W. Processing of gas-nitrided AISI 316L steel powder by laser powder bed fusion—Microstructure and properties. *Addit. Manuf.* **2019**, *30*, 100836. [CrossRef]
27. Hadraba, H.; Chlup, Z.; Dlouhy, A.; Dobes, F.; Roupcova, P.; Vilemova, M.; Matejicek, J. Oxide dispersion strengthened CoCrFeNiMn high-entropy alloy. *Mater. Sci. Eng. A* **2017**, *689*, 252–256. [CrossRef]
28. Li, B.; Qian, B.; Xu, Y.; Liu, Z.; Zhang, J.; Xuan, F. Additive manufacturing of ultrafine-grained austenitic stainless steel matrix composite via vanadium carbide reinforcement addition and selective laser melting: Formation mechanism and strengthening effect. *Mater. Sci. Eng. A* **2019**, *745*, 495–508. [CrossRef]
29. Li, W.; Yang, Y.; Liu, J.; Zhou, Y.; Li, M.; Wen, S.; Wei, Q.; Yan, C.; Shi, Y. Enhanced nanohardness and new insights into texture evolution and phase transformation of TiAl/TiB 2 in-situ metal matrix composites prepared via selective laser melting. *Acta Mater.* **2017**, *136*, 90–104. [CrossRef]
30. Dai, S.; Zhu, J.; Yan, X.; Wu, S.; Liu, Y.; Gao, X.; Fraser, H.; Hodgson, P.; Zhu, Y.; Heilmaier, M.; et al. Unique Yttria Nanoparticle Strengthening in an Inconel 718 Superalloy Fabricated by Additive Manufacturing. *Adv. Mater. Technol.* **2024**, *9*, 2301421. [CrossRef]
31. Xu, R.; Geng, Z.; Wu, Y.; Chen, C.; Ni, M.; Li, D.; Zhang, T.; Huang, H.; Liu, F.; Li, R.; et al. Microstructure and mechanical properties of in-situ oxide-dispersion-strengthened NiCrFeY alloy produced by laser powder bed fusion. *Adv. Powder Mater.* **2022**, *1*, 100056. [CrossRef]
32. Smith, T.M.; Kantzos, C.A.; Zarkevich, N.A.; Harder, B.J.; Heczko, M.; Gradl, P.R.; Thompson, A.C.; Mills, M.J.; Gabb, T.P.; Lawson, J.W. A 3D printable alloy designed for extreme environments. *Nature* **2023**, *617*, 513–518. [CrossRef]
33. Smith, T.M.; Thompson, A.C.; Gabb, T.P.; Bowman, C.L.; Kantzos, C.A. Efficient production of a high-performance dispersion strengthened, multi-principal element alloy. *Sci. Rep.* **2020**, *10*, 9663. [CrossRef] [PubMed]
34. Yu, L.; Lu, Z.; Xian, J.; Chen, X.; Peng, S.; Li, X.; Li, H. Effects of Al content on microstructure and tensile properties of Ni-based ODS superalloys. *J. Alloys Compd.* **2023**, *941*, 168965. [CrossRef]
35. Jang, J.; Kim, T.K.; Han, C.H.; Min, H.-K.; Jeong, S.-H.; Kim, D.H. A Preliminary Development and Characterization of Ni-based ODS Alloys. *Procedia Eng.* **2013**, *55*, 284–288. [CrossRef]
36. Mirzababaei, S.; Ghayoor, M.; Doyle, R.P.; Pasebani, S. In-situ manufacturing of ODS FeCrAlY alloy via laser powder bed fusion. *Mater. Lett.* **2021**, *284*, 129046. [CrossRef]
37. Ramakrishnan, T.; Espiritu, E.R.; Kwon, S.; Keshavarz, M.K.; Muniz-Lerma, J.A.; Gauvin, R.; Brochu, M. Laser powder bed fusion additive manufacturing of molybdenum using a nitrogen build atmosphere. *Int. J. Refract. Met. Hard Mater.* **2024**, *119*, 106555. [CrossRef]
38. Chen, P.; Yang, C.; Li, S.; Attallah, M.M.; Yan, M. In-situ alloyed, oxide-dispersion-strengthened CoCrFeMnNi high entropy alloy fabricated via laser powder bed fusion. *Mater. Des.* **2020**, *194*, 108966. [CrossRef]
39. Tjong, S.C. Novel Nanoparticle-Reinforced Metal Matrix Composites with Enhanced Mechanical Properties. *Adv. Eng. Mater.* **2007**, *9*, 639–652. [CrossRef]
40. Šulák, I.; Chlupová, A.; Záležák, T.; Kuběna, I.; Roth, J.-P.; Jahns, K.; Krupp, U.; Kruml, T. High-temperature Fatigue and Creep Performance of Additively Manufactured NiCu-based Alloy. *Procedia Struct. Integr.* **2024**, *52*, 143–153. [CrossRef]
41. Narayana Samy, V.P.; Brasche, F.; Šulák, I.; Verma, B.; Nowak, B.; Chlup, Z.; Záležák, T.; Schleifenbaum, J.H.; Krupp, U.; Haase, C. The influence of microstructural heterogeneities on high-temperature mechanical properties of additively manufactured γ'-forming Ni-based alloys. *Addit. Manuf.* **2024**, *88*, 104267. [CrossRef]
42. Meltzer, R.L.; Fiorini, Y.R.; Horstman, R.T.; Moore, I.C.; Batik, A.L.; Hostinsky, T.; Čadek, J. A Constant Tensile Stress Creep Testing Machine. *J. Test. Eval.* **1976**, *4*, 26. [CrossRef]
43. Rettenmayr, M. Melting and remelting phenomena. *Int. Mater. Rev.* **2009**, *54*, 1–17. [CrossRef]
44. Qi, H.; Zhou, X.; Li, J.; Hu, Y.; Xu, L. Performance Testing and Rapid Solidification Behavior of Stainless Steel Powders Prepared by Gas Atomization. *Materials* **2021**, *14*, 5188. [CrossRef] [PubMed]
45. Gao, C.; Xiao, Z.; Zou, H.; Liu, Z.; Chen, J.; Li, S.; Zhang, D. Characterization of spherical AlSi10Mg powder produced by double-nozzle gas atomization using different parameters. *Trans. Nonferrous Met. Soc. China* **2019**, *29*, 374–384. [CrossRef]
46. Priyadarshi, A.; Bin Shahrani, S.; Choma, T.; Zrodowski, L.; Qin, L.; Leung, C.L.A.; Clark, S.J.; Fezzaa, K.; Mi, J.; Lee, P.D.; et al. New insights into the mechanism of ultrasonic atomization for the production of metal powders in additive manufacturing. *Addit. Manuf.* **2024**, *83*, 104033. [CrossRef]
47. Pellicer, E.; Varea, A.; Sivaraman, K.M.; Pané, S.; Suriñach, S.; Baró, M.D.; Nogués, J.; Nelson, B.J.; Sort, J. Grain boundary segregation and interdiffusion effects in nickel-copper alloys: An effective means to improve the thermal stability of nanocrystalline nickel. *ACS Appl. Mater. Interfaces* **2011**, *3*, 2265–2274. [CrossRef]
48. Naghash, A.R.; Etsell, T.H.; Xu, S. XRD and XPS Study of Cu−Ni Interactions on Reduced Copper−Nickel−Aluminum Oxide Solid Solution Catalysts. *Chem. Mater.* **2006**, *18*, 2480–2488. [CrossRef]
49. Erdélyi, Z.; Girardeaux, C.; Tôkei, Z.; Beke, D.L.; Cserháti, C.; Rolland, A. Investigation of the interplay of nickel dissolution and copper segregation in Ni/Cu(111) system. *Surf. Sci.* **2002**, *496*, 129–140. [CrossRef]

50. Guler, U.; Suslov, S.; Kildishev, A.V.; Boltasseva, A.; Shalaev, V.M. Colloidal Plasmonic Titanium Nitride Nanoparticles: Properties and Applications. *Nanophotonics* **2015**, *4*, 269–276. [CrossRef]
51. Clatworthy, E.B.; Yick, S.; Murdock, A.T.; Allison, M.C.; Bendavid, A.; Masters, A.F.; Maschmeyer, T. Enhanced Photocatalytic Hydrogen Evolution with TiO 2 –TiN Nanoparticle Composites. *J. Phys. Chem. C* **2019**, *123*, 3740–3749. [CrossRef]
52. Alvarez Barragan, A.; Ilawe, N.V.; Zhong, L.; Wong, B.M.; Mangolini, L. A Non-Thermal Plasma Route to Plasmonic TiN Nanoparticles. *J. Phys. Chem. C* **2017**, *121*, 2316–2322. [CrossRef]
53. Tavares, J.; Coulombe, S.; Meunier, J.-L. Synthesis of cubic-structured monocrystalline titanium nitride nanoparticles by means of a dual plasma process. *J. Phys. D Appl. Phys.* **2009**, *42*, 102001. [CrossRef]
54. Chen, G.; Zhao, S.Y.; Tan, P.; Wang, J.; Xiang, C.S.; Tang, H.P. A comparative study of Ti-6Al-4V powders for additive manufacturing by gas atomization, plasma rotating electrode process and plasma atomization. *Powder Technol.* **2018**, *333*, 38–46. [CrossRef]
55. Yodoshi, N.; Endo, T.; Masahashi, N. Evaluation of Porosity in Gas-Atomized Powder by Synchrotron X-ray CT and Investigation of the Effect of Gas Species. *Mater. Trans.* **2021**, *62*, 1549–1555. [CrossRef]
56. Ruan, G.; Liu, C.; Qu, H.; Guo, C.; Li, G.; Li, X.; Zhu, Q. A comparative study on laser powder bed fusion of IN718 powders produced by gas atomization and plasma rotating electrode process. *Mater. Sci. Eng. A* **2022**, *850*, 143589. [CrossRef]
57. Liu, T.; Leazer, J.D.; Menon, S.K.; Brewer, L.N. Microstructural analysis of gas atomized Al-Cu alloy feedstock powders for cold spray deposition. *Surf. Coat. Technol.* **2018**, *350*, 621–632. [CrossRef]
58. Schwenck, D.; Ellendt, N.; Fischer-Bühner, J.; Hofmann, P.; Uhlenwinkel, V. A novel convergent–divergent annular nozzle design for close-coupled atomisation. *Powder Metall.* **2017**, *60*, 198–207. [CrossRef]
59. Mullis, A.M.; Farrell, L.; Cochrane, R.F.; Adkins, N.J. Estimation of Cooling Rates During Close-Coupled Gas Atomization Using Secondary Dendrite Arm Spacing Measurement. *Met. Mater. Trans. B* **2013**, *44*, 992–999. [CrossRef]
60. Ciftci, N.; Ellendt, N.; Coulthard, G.; Soares Barreto, E.; Mädler, L.; Uhlenwinkel, V. Novel Cooling Rate Correlations in Molten Metal Gas Atomization. *Met. Mater. Trans. B* **2019**, *50*, 666–677. [CrossRef]
61. Soares Barreto, E.; Frey, M.; Wegner, J.; Jose, A.; Neuber, N.; Busch, R.; Kleszczynski, S.; Mädler, L.; Uhlenwinkel, V. Properties of gas-atomized Cu-Ti-based metallic glass powders for additive manufacturing. *Mater. Des.* **2022**, *215*, 110519. [CrossRef]
62. Mani, C.; Karthikeyan, R.; Kannan, S. Electrochemical Impedance Analysis on Cryogenically Treated Dissimilar Metal Welding of 316L Stainless Steel and Monel 400 Alloy Using GTAW. *Metals* **2019**, *9*, 1088. [CrossRef]
63. Kostryzhev, A.G.; Marenych, O.O.; Pan, Z.; Li, H.; van Duin, S. Strengthening mechanisms in Monel K500 alloyed with Al and Ti. *J. Mater. Sci.* **2023**, *58*, 4150–4164. [CrossRef]
64. Tian, Y.T.; Li, Y.; Xia, L.; Man, T.H. Research on New Technology of Metal Powder-Plate Composite Rolling. *Int. Conf. Adv. Mater. Eng. Mater.* **2020**, *861*, 41–45. [CrossRef]
65. Wei, P.; Chen, Z.; Zhang, S.; Li, B.; Han, J.; Lu, B. Microstructure and mechanical properties of graphene and nano-zirconia reinforced AlSi10Mg composite fabricated by laser powder bed fusion. *Mater. Sci. Eng. A* **2023**, *864*, 144574. [CrossRef]
66. Doñate-Buendia, C.; Kürnsteiner, P.; Stern, F.; Wilms, M.B.; Streubel, R.; Kusoglu, I.M.; Tenkamp, J.; Bruder, E.; Pirch, N.; Barcikowski, S.; et al. Microstructure formation and mechanical properties of ODS steels built by laser additive manufacturing of nanoparticle coated iron-chromium powders. *Acta Mater.* **2021**, *206*, 116566. [CrossRef]
67. Zhang, Z.; Chen, D.L. Contribution of Orowan strengthening effect in particulate-reinforced metal matrix nanocomposites. *Mater. Sci. Eng. A* **2008**, *483–484*, 148–152. [CrossRef]
68. Kang, Y.; Han, Q.; Zhao, X.; Cai, M. Influence of nanoparticle reinforcements on the strengthening mechanisms of an ultrafine-grained dual phase steel containing titanium. *Mater. Des.* **2013**, *44*, 331–339. [CrossRef]
69. Zou, L.; Yang, C.; Lei, Y.; Zakharov, D.; Wiezorek, J.M.K.; Su, D.; Yin, Q.; Li, J.; Liu, Z.; Stach, E.A.; et al. Dislocation nucleation facilitated by atomic segregation. *Nat. Mater.* **2018**, *17*, 56–63. [CrossRef]
70. Marenych, O.O.; Ding, D.; Pan, Z.; Kostryzhev, A.G.; Li, H.; van Duin, S. Effect of chemical composition on microstructure, strength and wear resistance of wire deposited Ni-Cu alloys. *Addit. Manuf.* **2018**, *24*, 30–36. [CrossRef]
71. Kannan, A.R.; Kumar, S.M.; Pramod, R.; Shanmugam, N.S.; Vishnukumar, M.; Channabasavanna, S.G. Microstructure and corrosion resistance of Ni-Cu alloy fabricated through wire arc additive manufacturing. *Mater. Lett.* **2022**, *308*, 131262. [CrossRef]
72. Marenych, O.; Kostryzhev, A. Strengthening Mechanisms in Nickel-Copper Alloys: A Review. *Metals* **2020**, *10*, 1358. [CrossRef]
73. Ting, J.; Peretti, M.W.; Eisen, W.B. The effect of wake-closure phenomenon on gas atomization performance. *Mater. Sci. Eng. A* **2002**, *326*, 110–121. [CrossRef]
74. Vedovato, G.; Zambon, A.; Ramous, E. A simplified model for gas atomization. *Mater. Sci. Eng. A* **2001**, *304–306*, 235–239. [CrossRef]
75. Tourret, D.; Reinhart, G.; Gandin, C.-A.; Iles, G.N.; Dahlborg, U.; Calvo-Dahlborg, M.; Bao, C.M. Gas atomization of Al–Ni powders: Solidification modeling and neutron diffraction analysis. *Acta Mater.* **2011**, *59*, 6658–6669. [CrossRef]
76. Ertay, D.S.; Ma, H.; Vlasea, M. *Correlative Beam Path and Pore Defect Space Analysis for Modulated Powder Bed Laser Fusion Process*; Solid Freeform Fabrication Symposium, University of Texas at Austin: Austin, TX, USA, 2018.
77. Ulbricht, A.; Mohr, G.; Altenburg, S.J.; Oster, S.; Maierhofer, C.; Bruno, G. Can Potential Defects in LPBF Be Healed from the Laser Exposure of Subsequent Layers? A Quantitative Study. *Metals* **2021**, *11*, 1012. [CrossRef]

78. Hojjatzadeh, S.M.H.; Parab, N.D.; Guo, Q.; Qu, M.; Xiong, L.; Zhao, C.; Escano, L.I.; Fezzaa, K.; Everhart, W.; Sun, T.; et al. Direct observation of pore formation mechanisms during LPBF additive manufacturing process and high energy density laser welding. *Int. J. Mach. Tools Manuf.* **2020**, *153*, 103555. [CrossRef]
79. Kan, W.H.; Chiu, L.N.S.; Lim, C.V.S.; Zhu, Y.; Tian, Y.; Jiang, D.; Huang, A. A critical review on the effects of process-induced porosity on the mechanical properties of alloys fabricated by laser powder bed fusion. *J. Mater. Sci.* **2022**, *57*, 9818–9865. [CrossRef]
80. Kan, W.H.; Gao, M.; Zhang, X.; Liang, E.; Chiu, N.S.L.; Lim, C.V.S.; Huang, A. The influence of porosity on Ti-6Al-4V parts fabricated by laser powder bed fusion in the pursuit of process efficiency. *Int. J. Adv. Manuf. Technol.* **2022**, *119*, 5417–5438. [CrossRef]
81. Voisin, T.; Calta, N.P.; Khairallah, S.A.; Forien, J.-B.; Balogh, L.; Cunningham, R.W.; Rollett, A.D.; Wang, Y.M. Defects-dictated tensile properties of selective laser melted Ti-6Al-4V. *Mater. Des.* **2018**, *158*, 113–126. [CrossRef]
82. Huang, Y.; Fleming, T.G.; Clark, S.J.; Marussi, S.; Fezzaa, K.; Thiyagalingam, J.; Leung, C.L.A.; Lee, P.D. Keyhole fluctuation and pore formation mechanisms during laser powder bed fusion additive manufacturing. *Nat. Commun.* **2022**, *13*, 1170. [CrossRef]
83. Li, C.; White, R.; Fang, X.Y.; Weaver, M.; Guo, Y.B. Microstructure evolution characteristics of Inconel 625 alloy from selective laser melting to heat treatment. *Mater. Sci. Eng. A* **2017**, *705*, 20–31. [CrossRef]
84. Pilz, S.; Gustmann, T.; Günther, F.; Zimmermann, M.; Kühn, U.; Gebert, A. Controlling the Young's modulus of a ß-type Ti-Nb alloy via strong texturing by LPBF. *Mater. Des.* **2022**, *216*, 110516. [CrossRef]
85. Avateffazeli, M.; Carrion, P.E.; Shachi-Amirkhiz, B.; Pirgazi, H.; Mohammadi, M.; Shamsaei, N.; Haghshenas, M. Correlation between tensile properties, microstructure, and processing routes of an Al–Cu–Mg–Ag–TiB2 (A205) alloy: Additive manufacturing and casting. *Mater. Sci. Eng. A* **2022**, *841*, 142989. [CrossRef]
86. Krakhmalev, P.; Fredriksson, G.; Svensson, K.; Yadroitsev, I.; Yadroitsava, I.; Thuvander, M.; Peng, R. Microstructure, Solidification Texture, and Thermal Stability of 316 L Stainless Steel Manufactured by Laser Powder Bed Fusion. *Metals* **2018**, *8*, 643. [CrossRef]
87. Cordero, Z.C.; Knight, B.E.; Schuh, C.A. Six decades of the Hall–Petch effect—A survey of grain-size strengthening studies on pure metals. *Int. Mater. Rev.* **2016**, *61*, 495–512. [CrossRef]
88. Zhao, Y.; Ma, T.; Gao, Z.; Feng, Y.; Li, C.; Guo, Q.; Ma, Z.; Liu, Y. Significant reduction of grain size and texture intensity in laser powder bed fusion fabricated nickel-based superalloy by increasing constitutional supercooling. *Compos. Part B Eng.* **2023**, *266*, 111040. [CrossRef]
89. Muránsky, O.; Balogh, L.; Tran, M.; Hamelin, C.J.; Park, J.-S.; Daymond, M.R. On the measurement of dislocations and dislocation substructures using EBSD and HRSD techniques. *Acta Mater.* **2019**, *175*, 297–313. [CrossRef]
90. Smith, J.; Xiong, W.; Yan, W.; Lin, S.; Cheng, P.; Kafka, O.L.; Wagner, G.J.; Cao, J.; Liu, W.K. Linking process, structure, property, and performance for metal-based additive manufacturing: Computational approaches with experimental support. *Comput. Mech.* **2016**, *57*, 583–610. [CrossRef]
91. Zhang, X.X.; Andrä, H.; Harjo, S.; Gong, W.; Kawasaki, T.; Lutz, A.; Lahres, M. Quantifying internal strains, stresses, and dislocation density in additively manufactured AlSi10Mg during loading-unloading-reloading deformation. *Mater. Des.* **2021**, *198*, 109339. [CrossRef]
92. Voisin, T.; Forien, J.-B.; Perron, A.; Aubry, S.; Bertin, N.; Samanta, A.; Baker, A.; Wang, Y.M. New insights on cellular structures strengthening mechanisms and thermal stability of an austenitic stainless steel fabricated by laser powder-bed-fusion. *Acta Mater.* **2021**, *203*, 116476. [CrossRef]
93. Kong, D.; Dong, C.; Wei, S.; Ni, X.; Zhang, L.; Li, R.; Wang, L.; Man, C.; Li, X. About metastable cellular structure in additively manufactured austenitic stainless steels. *Addit. Manuf.* **2021**, *38*, 101804. [CrossRef]
94. Bertsch, K.M.; Meric de Bellefon, G.; Kuehl, B.; Thoma, D.J. Origin of dislocation structures in an additively manufactured austenitic stainless steel 316L. *Acta Mater.* **2020**, *199*, 19–33. [CrossRef]
95. Gao, C.; Wang, Z.; Xiao, Z.; You, D.; Wong, K.; Akbarzadeh, A.H. Selective laser melting of TiN nanoparticle-reinforced AlSi10Mg composite: Microstructural, interfacial, and mechanical properties. *J. Mater. Process. Technol.* **2020**, *281*, 116618. [CrossRef]
96. Jena, A.; Atabay, S.E.; Gontcharov, A.; Lowden, P.; Brochu, M. Laser powder bed fusion of a new high gamma prime Ni-based superalloy with improved weldability. *Mater. Des.* **2021**, *208*, 109895. [CrossRef]
97. Huang, Z.; Zhai, Z.; Lin, W.; Chang, H.; Wu, Y.; Yang, R.; Zhang, Z. On the orientation dependent microstructure and mechanical behavior of Hastelloy X superalloy fabricated by laser powder bed fusion. *Mater. Sci. Eng. A* **2022**, *844*, 143208. [CrossRef]
98. Qin, H.; Dong, Q.; Fallah, V.; Daymond, M.R. Rapid Solidification and Non-equilibrium Phase Constitution in Laser Powder Bed Fusion (LPBF) of AlSi10Mg Alloy: Analysis of Nano-precipitates, Eutectic Phases, and Hardness Evolution. *Met. Mater. Trans. A* **2020**, *51*, 448–466. [CrossRef]
99. Li, J.; Cheng, T.; Liu, Y.; Yang, Y.; Li, W.; Wei, Q. Simultaneously enhanced strength and ductility of Cu-15Ni-8Sn alloy with periodic heterogeneous microstructures fabricated by laser powder bed fusion. *Addit. Manuf.* **2022**, *54*, 102726. [CrossRef]
100. Song, Z.; Gao, S.; Wang, Z.; Lan, L.; Hou, J.; He, B. Effects of non-equilibrium microstructures on microstructure evolution and mechanical properties of laser powder bed fusion IN625 Ni-based superalloy during long-term thermal exposure at 700 °C and 750 °C. *Mater. Sci. Eng. A* **2022**, *856*, 143883. [CrossRef]
101. Jodi, D.E.; Kitashima, T.; Singh, A.; Watanabe, M. High-temperature microstructural stability of pure Ni fabricated by laser powder bed fusion using Gaussian and flat-top beam profiles. *Mater. Charact.* **2023**, *200*, 112897. [CrossRef]

102. Bassini, E.; Sivo, A.; Martelli, P.A.; Rajczak, E.; Marchese, G.; Calignano, F.; Biamino, S.; Ugues, D. Effects of the solution and first aging treatment applied to as-built and post-HIP CM247 produced via laser powder bed fusion (LPBF). *J. Alloys Compd.* **2022**, *905*, 164213. [CrossRef]
103. Hatakeyama, T.; Sawada, K.; Suzuki, M.; Watanabe, M. Microstructure development of modified 9Cr-1Mo steel during laser powder bed fusion and heat treatment. *Addit. Manuf.* **2023**, *61*, 103350. [CrossRef]
104. Jiang, R.; Mostafaei, A.; Wu, Z.; Choi, A.; Guan, P.-W.; Chmielus, M.; Rollett, A.D. Effect of heat treatment on microstructural evolution and hardness homogeneity in laser powder bed fusion of alloy 718. *Addit. Manuf.* **2020**, *35*, 101282. [CrossRef]
105. Okugawa, M.; Saito, K.; Yoshima, H.; Sawaizumi, K.; Nomoto, S.; Watanabe, M.; Nakano, T.; Koizumi, Y. Solute segregation in a rapidly solidified Hastelloy-X Ni-based superalloy during laser powder bed fusion investigated by phase-field and computational thermal-fluid dynamics simulations. *Addit. Manuf.* **2024**, *84*, 104079. [CrossRef]
106. Seede, R.; Zhang, B.; Whitt, A.; Picak, S.; Gibbons, S.; Flater, P.; Elwany, A.; Arroyave, R.; Karaman, I. Effect of heat treatments on the microstructure and mechanical properties of an ultra-high strength martensitic steel fabricated via laser powder bed fusion additive manufacturing. *Addit. Manuf.* **2021**, *47*, 102255. [CrossRef]
107. Gu, D.; Zhang, H.; Dai, D.; Xia, M.; Hong, C.; Poprawe, R. Laser additive manufacturing of nano-TiC reinforced Ni-based nanocomposites with tailored microstructure and performance. *Compos. Part B Eng.* **2019**, *163*, 585–597. [CrossRef]
108. Marenych, O.O.; Kostryzhev, A.G.; Pan, Z.; Li, H.; van Duin, S. Comparative effect of Mn/Ti solute atoms and TiC/Ni3(Al,Ti) nano-particles on work hardening behaviour in Ni Cu alloys fabricated by wire arc additive manufacturing. *Mater. Sci. Eng. A* **2019**, *753*, 262–275. [CrossRef]
109. Mukhopadhyay, A.; Urkude, D.K.; Mukhopadhyay, G. Effect of Cold Work on Hydrogen Embrittlement of Monel-400. *J. Fail. Anal. Preven.* **2024**, *24*, 279–290. [CrossRef]
110. Janardhan, G.; Kishore, K.; Dutta, K.; Mukhopadhyay, G. Tensile and fatigue behavior of resistance spot-welded HSLA steel sheets: Effect of pre-strain in association with dislocation density. *Mater. Sci. Eng. A* **2020**, *793*, 139796. [CrossRef]
111. Jeong, W.C. Effect of prestrain on aging and bake hardening of cold-rolled, continuously annealed steel sheets. *Met. Mater. Trans. A* **1998**, *29*, 463–467. [CrossRef]
112. Smith, B.A.; Laursen, C.M.; Bartanus, J.; Carroll, J.D.; Pataky, G.J. The Interplay of Geometric Defects and Porosity on the Mechanical Behavior of Additively Manufactured Components. *Exp. Mech.* **2021**, *61*, 685–698. [CrossRef]
113. Yin, D.; Liu, H.; Chen, Y.; Yi, D.; Wang, B.; Wang, B.; Shen, F.; Fu, S.; Tang, C.; Pan, S. Effect of grain size on fatigue-crack growth in 2524 aluminium alloy. *Int. J. Fatigue* **2016**, *84*, 9–16. [CrossRef]
114. Boissonnet, G.; Boulesteix, C.; Bonnet, G.; Balmain, J.; Pedraza, F. Thermal Transport Properties of New Coatings on Steels for Supercritical Steam Power Plants. *Oxid. Met.* **2017**, *88*, 191–202. [CrossRef]
115. Boissonnet, G.; Bonnet, G.; Pasquet, A.; Bourhila, N.; Pedraza, F. Evolution of thermal insulation of plasma-sprayed thermal barrier coating systems with exposure to high temperature. *J. Eur. Ceram. Soc.* **2019**, *39*, 2111–2121. [CrossRef]
116. Boissonnet, G.; Bonnet, G.; Pedraza, F. Thermo-Physical Properties of HR3C and P92 Steels at High-Temperature. *J. Mater. Appl.* **2019**, *8*, 59–64. [CrossRef]